Theses and Dissertations   1. Thesis and Dissertation Collection, all items

2006-09

Characterization and application of four-layer semiconductor structures in pulse mode operation

Matos, Antonio P.

Monterey, California. Naval Postgraduate School

http://hdl.handle.net/10945/2569

NAVAL POSTGRADUATE SCHOOL

MONTEREY, CALIFORNIA

THESIS

CHARACTERIZATION AND APPLICATION OF FOUR-LAYER SEMICONDUCTOR STRUCTURES IN PULSE MODE OPERATION

by

Antonio P. Matos

September 2006

Thesis Advisor: Gamani Karunasiri
Thesis Co-Advisor: James H. Luscombe

Approved for public release; distribution is unlimited

THIS PAGE INTENTIONALLY LEFT BLANK

REPORT DOCUMENTATION PAGE		*Form Approved OMB No. 0704-0188*
Public reporting burden for this collection of information is estimated to average 1 hour per response, including the time for reviewing instruction, searching existing data sources, gathering and maintaining the data needed, and completing and reviewing the collection of information. Send comments regarding this burden estimate or any other aspect of this collection of information, including suggestions for reducing this burden, to Washington headquarters Services, Directorate for Information Operations and Reports, 1215 Jefferson Davis Highway, Suite 1204, Arlington, VA 22202-4302, and to the Office of Management and Budget, Paperwork Reduction Project (0704-0188) Washington DC 20503.		
1. AGENCY USE ONLY *(Leave blank)*	**2. REPORT DATE** September 2006	**3. REPORT TYPE AND DATES COVERED** Master's Thesis
4. TITLE AND SUBTITLE Characterization and Application of Four-Layer Semiconductor Structures in Pulse Mode Operation.		**5. FUNDING NUMBERS**
6. AUTHOR(S) Antonio P. Matos		
7. PERFORMING ORGANIZATION NAME(S) AND ADDRESS(ES) Naval Postgraduate School Monterey, CA 93943-5000		**8. PERFORMING ORGANIZATION REPORT NUMBER**
9. SPONSORING /MONITORING AGENCY NAME(S) AND ADDRESS(ES) Space and Naval Warfare Systems Center, San Diego 52560 Hull St. San Diego, CA 92152-5001		**10. SPONSORING/MONITORING AGENCY REPORT NUMBER**
11. SUPPLEMENTARY NOTES The views expressed in this thesis are those of the author and do not reflect the official policy or position of the Department of Defense or the U.S. Government.		
12a. DISTRIBUTION / AVAILABILITY STATEMENT Approved for public release; distribution is unlimited.		**12b. DISTRIBUTION CODE** A
13. ABSTRACT (maximum 200 words) The characteristics and application of a thyristor (a four-layer semiconductor structure) in a pulse generating circuit are explored. A thyristor device was used to create a pulse generating circuit and the pulse interval duration of this circuit was experimentally measured. The pulse interval duration was determined to be characterized by a Poisson Point Process distribution that is dependent on both temperature and applied voltage bias. The adjustable aperiodicity of the pulse intervals was a key characteristic used to design a distributed processing system of micro-robots that are capable of swarming. A micro-robotic swarm platform was simulated using finite element analysis, a JAVA-based swarm model, and three fully operational macro-scale platforms.		
14. SUBJECT TERMS Thyristor, SCR, Pulse Mode Operation, Poisson Point Process, Micro-robotics, Emergent Behavior, Swarming, COMSOL		**15. NUMBER OF PAGES** 89
		16. PRICE CODE
17. SECURITY CLASSIFICATION OF REPORT Unclassified	**18. SECURITY CLASSIFICATION OF THIS PAGE** Unclassified	**19. SECURITY CLASSIFICATION OF ABSTRACT** Unclassified **20. LIMITATION OF ABSTRACT** UL

THIS PAGE INTENTIONALLY LEFT BLANK

CHARACTERIZATION AND APPLICATION OF FOUR-LAYER SEMICONDUCTOR STRUCTURES IN PULSE MODE OPERATION

Antonio P. Matos
Lieutenant, United States Navy
B.S., Worcester Polytechnic Institute, 1999

Submitted in partial fulfillment of the
requirements for the degree of

MASTER OF SCIENCE IN PHYSICS

from the

**NAVAL POSTGRADUATE SCHOOL
September 2006**

Author: Antonio P. Matos

Approved by: Gamani Karunasiri
                   Thesis Advisor

                   James H. Luscombe
                   Thesis Co-Advisor

                   James L. Kays
                   Dean, Graduate School of Engineering and Applied Sciences

iii

THIS PAGE INTENTIONALLY LEFT BLANK

ABSTRACT

The characteristics and application of a thyristor (a four-layer semiconductor structure) in a pulse generating circuit are explored. A thyristor device was used to create a pulse generating circuit and the pulse interval duration of this circuit was experimentally measured. The pulse interval duration was determined to be characterized by a Poisson Point Process distribution that is dependent on both temperature and applied voltage bias. The adjustable aperiodicity of the pulse intervals was a key characteristic used to design a distributed processing system of micro-robots that are capable of swarming. A micro-robotic swarm platform was simulated using finite element analysis, a JAVA-based swarm model, and three fully operational macro-scale platforms.

THIS PAGE INTENTIONALLY LEFT BLANK

TABLE OF CONTENTS

LIST OF FIGURES

x

THIS PAGE INTENTIONALLY LEFT BLANK

THIS PAGE INTENTIONALLY LEFT BLANK

EXECUTIVE SUMMARY

A four-layer (PNPN) semiconductor structure commonly known as silicon controlled rectifier (SCR) or thyristor can be used to create a pulse generation circuit by connecting it in series with a parallel resistor and capacitor. Previous work by Karunasiri has shown that the pulse generation of this circuit appears to have elements of both periodicity and randomness [1]. In this thesis, a detailed experimental study of the dependence of pulse rate with external bias and temperature are presented. The pulse interval duration can be characterized by a Poisson Point Process distribution that is dependent on both temperature and applied voltage bias.

In addition, the aperiodicity of the interval between pulses can be used in a distributed processing system such as a micro-robotic swarm. Individual elements can be biased to perform random-walk operations in the absence of external stimuli. When stimuli are present, the individual elements can transition to periodic, goal-seeking routines. In this manner, a system capable of emergent behavior can be constructed from extremely simple circuitry. The advantages of a distributed processing system are that it can have very small elements that can penetrate unobserved into very sensitive places and that it is highly adaptive to a rapidly changing environment.

The most important feature of the thyristor circuit is its scalability to very small dimensions. The fact that it is composed of three elements reduces the weight and cost of circuitry needed for a micro-robotic platform capable of swarming. The thyristor circuit is also an analog signal processor, which makes it fast and highly responsive to changing stimuli. Proof of concept of this distributed processing logic was observed through the use of macro-scale swarm platforms and a large-swarm computer simulation.

The design of the micro-robotic platform was created using standard CMOS, MEMS and RIMS processes and tested with the aid of finite element analysis. The design presented is ready for fabrication.

THIS PAGE INTENTIONALLY LEFT BLANK

I.   INTRODUCTION

The purpose of this thesis was to characterize the behavior of a PNPN device in a pulse generating circuit and then apply the results to a useful application. The first goal of this thesis is to show that the pulse interval distribution is dependent on temperature and bias voltage, and that the distribution of pulse intervals is described by a Poisson Point Process model. The second goal of this thesis is to use the unique characteristics of the pulse generating circuit to design a distributed processing system of micro-robots that are capable of swarming.

This chapter gives a brief introduction to the physics of pulse generation using a PNPN device and outlines some previous experimental evidence of the aperiodic nature of the pulse intervals. This is followed by a description of the data collection method used to study the dependence of inter-pulse duration on temperature and voltage bias. The second chapter of the thesis describes the observed pulse rate dependence on temperature and bias voltage. This is followed by an analysis of this behavior using a statistical model and chaos. The third chapter presents an application of the unique characteristics of the thyristor circuit to a distributed processing system capable of swarming. The final chapter summarizes the results of this thesis and suggests some ideas for future research.

A.   ORIGIN OF PULSE GENERATION

The spontaneous generation of voltage pulses in response to a DC bias is of particular interest in applications that require pulse mode logic. The archetype for this behavior is the retinal neuron which operates as a pulse mode optical sensor. A similar spontaneous pulse generation can be achieved with a four-layer semiconductor device.

Spontaneous generation of voltage pulses was observed in a circuit that consists of an SCR in series with a parallel RC circuit under a DC bias. The pulse rate was found to increase with the DC bias and saturated as the pulse period reached the RC time constant. Injection of current into the gate was also found to increase the pulse rate [1]. Figure 1 shows a schematic of a typical pulse generation circuit used.
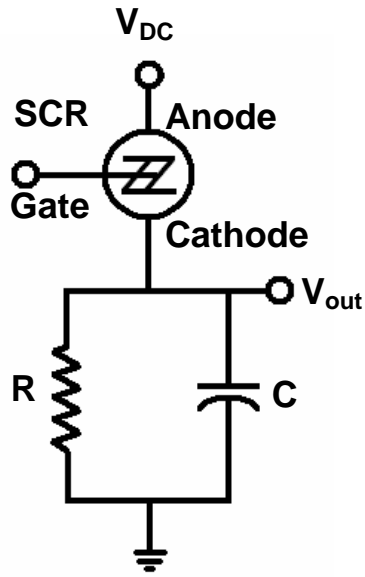
Figure 1.   SCR circuit schematic.

In the off state, the SCR acts as an open and the capacitor drains off its charge through the resistor. When enough charge is depleted, the capacitor has a low enough voltage across it that the SCR can switch on, if the voltage across it exceeds the threshold voltage. When the SCR turns on, the charge on the capacitor fills up much faster than it can discharge through the resistor and the voltage across the SCR reduces until it is forced to turn back off. The process repeats.

Karunasiri [1] explains the switching behavior of the SCR as follows:

As the DC bias across the SCR approaches the switching voltage, the injection of electrons and holes into the middle reverse biased p-n junction by the two outer forward biased p-n junctions rapidly increases as illustrated by the band diagram (in the inset of Fig. 2). These injected carriers sweep across the middle p-n junction and accumulate in the potential wells formed near the outer two p-n junctions as shown by the band diagram of the SCR (see the inset of Fig. 2). These accumulated charges tend to attract additional charge carriers with opposite polarity from the two outmost layers and the process quickly becomes regenerative. The accumulation of charges generates an increasing electric field in the middle p-n junction opposite to that of the applied bias causing it to forward bias sending the SCR to the ON state [1].
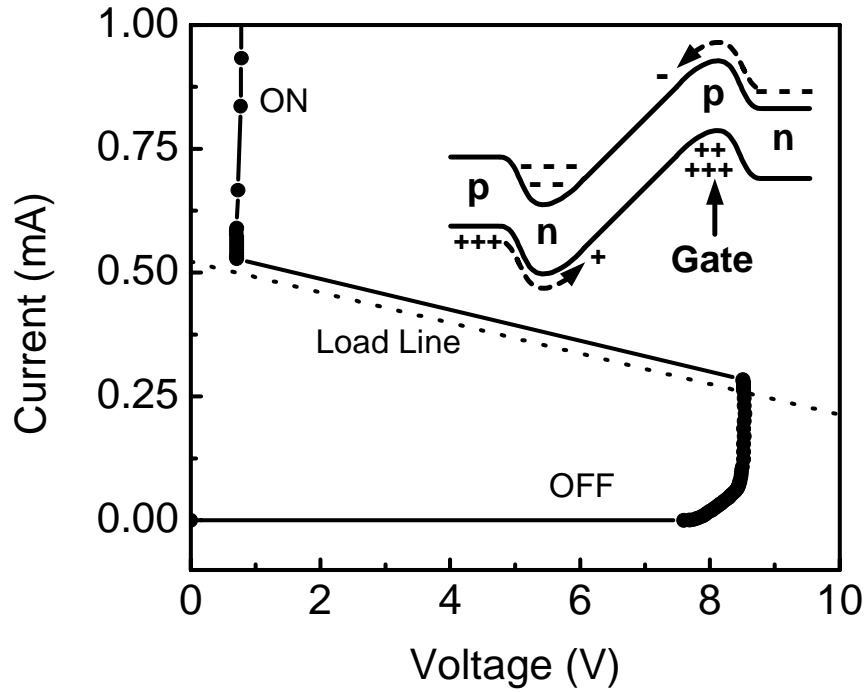
Figure 2.   (Taken from Ref. [1]) Measured current-voltage (I-V) characteristics of the SCR showing the on and off states. The switching voltage of the SCR is about 8.5 V. The inset shows the schematic band diagram and charge accumulation in the SCR just below the switching voltage (in the off state). The dashed line shows the load line of the circuit.

This theory is derived from PN Hook Theory, which was first introduced in 1950 by William Shockley to describe the switching mechanism of a PNPN device [2].

B.   SUMMARY OF PREVIOUS EXPERIMENTAL RESULTS

In order to properly bias the SCR circuit for sustained pulsing operation, the capacitance must be chosen to be big enough to provide a low impedance path ($\sim 1\ \Omega$) given the switching rise time and the peak transient current (CV_p / τ) of the thyristor. The resistor must be chosen to be small enough to maintain the current needed for switching and large enough to keep the current below the holding current of the thyristor [1].

The observation of interest is that the inter-pulse time duration does not depend solely on the RC time constant as expected. Rather, it is intrinsic to the SCR and the strength of the DC bias across the circuit. The inter-pulse duration can be arbitrarily

increased by reducing the DC bias across the circuit. At low bias, the rate of injection of minority carriers into the reverse biased middle p-n junction is relatively small which in turn slows the regenerative process and hence increases the time required for generating the electric field necessary for switching the SCR. This is also responsible for the aperiodic nature of the time intervals between pulses [1]. Figure 3 shows typical observed voltage outputs for the thyristor circuit for high DC bias (periodic) pulses and low DC bias (aperiodic) pulses.
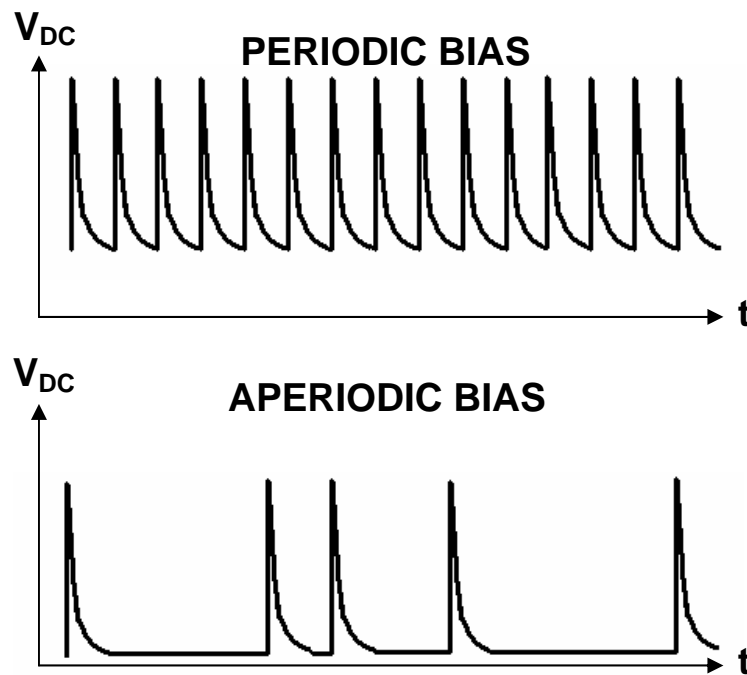
Figure 3.   Typical observed sequences of pulses as a function of time or high DC bias (top) and low DC bias (bottom). The pulse height is approximately equal to the switching voltage of the SCR.

The pulse rate prior to saturation (due to the RC time constant of the circuit) is determined by the amount of current injected into the middle PN junction by the two forward biased outer PN junctions. The bias dependence of the injected current can be obtained using the standard diode equation and thus the average frequency dependence on bias is expressed as

$$\langle f \rangle = f_0 \exp\left(\frac{e\left(V_{SCR} - V_T\right)}{\eta kT} \right) \tag{1.1}$$

where η is the ideality factor, f_0 is a parameter, and V_T is the threshold voltage for pulsing which depends on the switching voltage of the SCR [1]. By taking the inverse of both sides, the average time interval dependence of the PNPN device as a function of applied bias can be understood as follows:

$$\langle t \rangle = t_0 \exp\left(\frac{-e\left(V_{SCR} - V_T\right)}{\eta kT} \right) \tag{1.2}$$

where $t_0 = \dfrac{1}{f_0}$ is related to the RC time constant.

C.   DATA COLLECTION METHOD

The purpose of data collection was to measure the pulse rate dependence of a thyristor circuit on temperature and voltage bias. It was also desired to examine the variation of inter-pulse time delay for a large time series of data at a constant temperature and voltage bias. It was determined that the best way to achieve these objectives was to record the time interval between pulse peaks.

Data collection was conducted on the Motorola MBS4991 Silicon Bilateral Switch (SBS) connected to parallel RC circuit with C = 30 nF and R= 33 kΩ. This is a 4 layer PNPN thyristor device that exhibits pulse generation with random pulse intervals. Figure 4 shows the functional setup used for data collection.
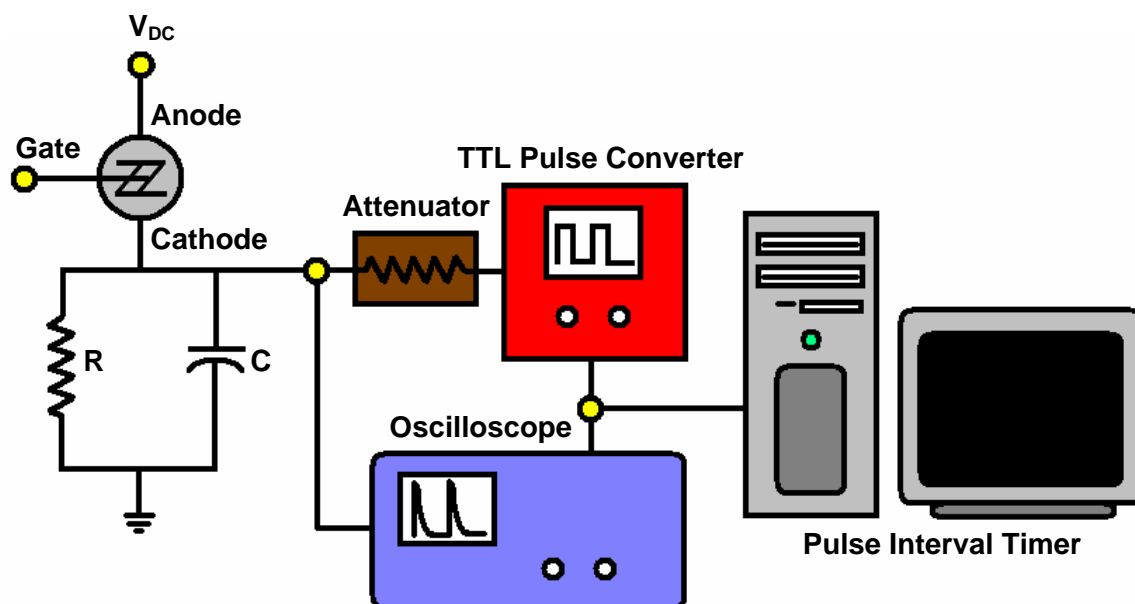
Figure 4.   Experimental setup used for the measurement of a time series of pulses.

The pulse generating circuit signal was fed through an attenuator into a TTL Pulse Converter which took the input of 16 V pulses and converted them to 5 V TTL pulses. This step is necessary since the pulses from the circuit are not capable of driving the counter directly. This TTL output was used as an input to a Pulse Interval Timer data acquisition program written in LABVIEW. The pulse interval times were recorded for 65536 pulses per series. Each series was chosen for a particular temperature and DC bias. Temperature was manually controlled by the use of a thermo-electric heater/cooler with an accuracy of ± 1 F. Voltage was automatically controlled via a Keithly 230 Programmable Voltage Source with an interface to LABVIEW.

An Agilent Infiniium Oscilloscope (1 GSa/sec) was used to record the average voltage waveform characteristics of 32 pulses per series. Figure 5 shows a typical voltage waveform output recorded by the Oscilloscope for a circuit with a 1 ms RC time constant. The yellow line is the voltage output across the resistor and the green line is the TTL conversion of the signal used for counting.

6
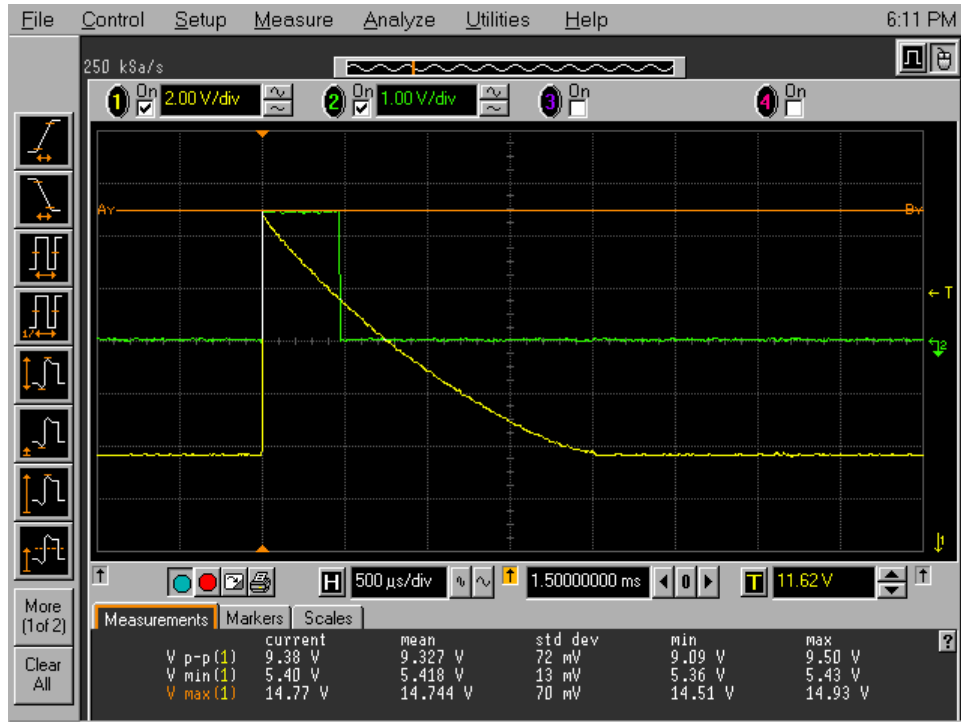
Figure 5.　　Voltage output across the resistor (yellow trace) and the corresponding TTL pulse (green trace).

1.　　LABVIEW Control

The acquisition of pulse interval time was facilitated by the use of a computer control system. The 5V TTL pulses were fed into the computer via a National Instruments SCB-68 Counter/Timer PCI Board. The accuracy of the timer was set to $\pm 10 \mu s$. The pulse interval times were recorded via a LABVIEW Virtual Instrument script and output to a file tagged with the DC bias voltage and temperature information. For series with long pulse interval times, the number of counts attained was less than 65536 because the total data acquisition time for each series was restricted to 24 hrs.

The DC bias was also computer controlled via a PCIB interface to the Keithly 230 Programmable Voltage Source. The power supply was accurate up to ± 1 mV and could be computer controlled by 0.05 V increments.

2.　　SBS Characteristics

The switching voltage of the MBS4991 was experimentally determined by the use of an Agilent 4155B Semiconductor Parameter Analyzer. Figure 6 shows the observed I-V characteristics of the device.

7
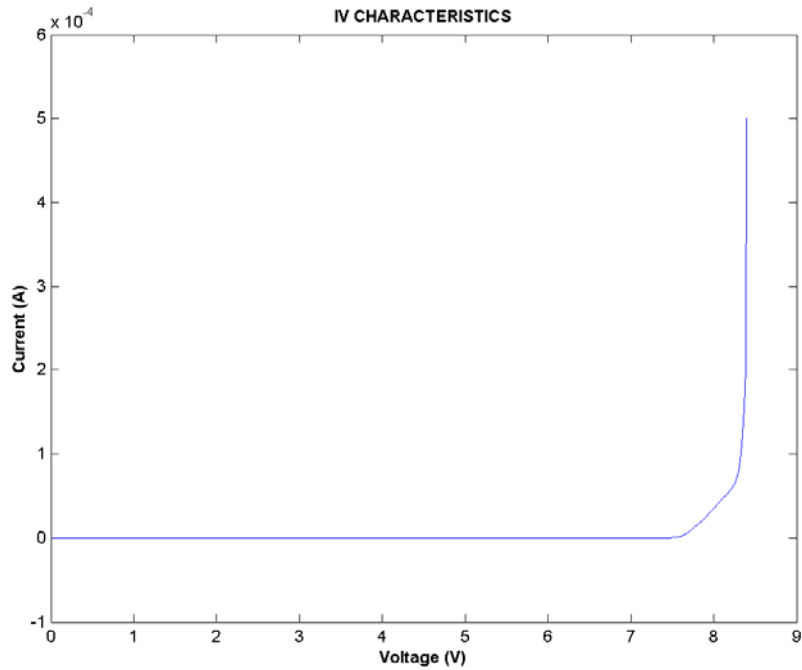
Figure 6.   I-V Characteristics of the MBS4991.

The Switching Voltage is about 8.42 V at a room temperature of approximately 65 F. The manufacturer data sheet shows that the switching voltage has an approximately linear dependence on temperature [2]. This dependence was experimentally verified for the range of temperatures 60-68 F. Figure 7 shows the experimentally determined results. It appears that the switching voltage remains relatively constant over the range of temperatures used.
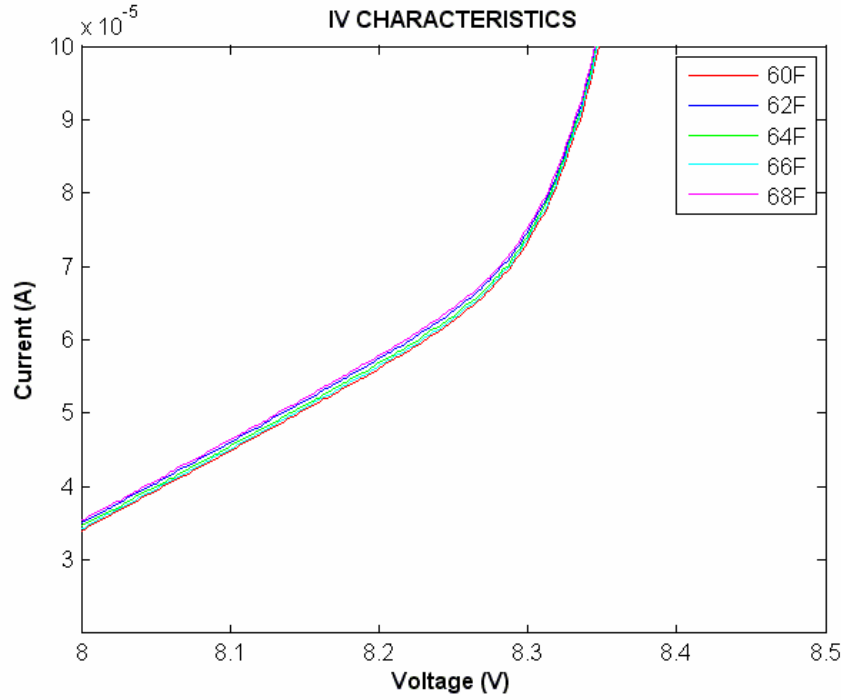
Figure 7.   Temperature dependence of switching voltage (use the same y-axis
format as the Fig. 6).

3.   Pulse Generating Circuit Characteristics

The SBS was placed in series with a parallel resistor and capacitor circuit. The resistance value chosen was 33 kΩ. This resistance was small enough to maintain the current needed for switching and large enough to keep the current below the holding current of the SBS. The capacitance value chosen was 30 nF which was big enough to provide a low impedance path for the peak transient current during switching. The RC time constant of the circuit is about 1 ms.

This time constant was experimentally observed to be the refractory period for the pulse generating circuit. During this time, no pulses were observed in any of the series.

THIS PAGE INTENTIONALLY LEFT BLANK

II.   THYRISTOR CIRCUIT CHARATERISTICS

This chapter discusses the observed pulse rate dependence on temperature and bias voltage of an SBS circuit. This is followed by an analysis of this behavior using a Poison Point Process statistical model and chaos. The goal is to show that the spontaneous pulse generation observed can be classified as a memoryless process similar to that observed in action potentials of some biological neurons [4].

In order to measure the pulse rate dependence on voltage bias and temperature, the interval times between pulses was recorded for a set of bias and temperature values. Figure 8 is a typical output as a function of recording time.
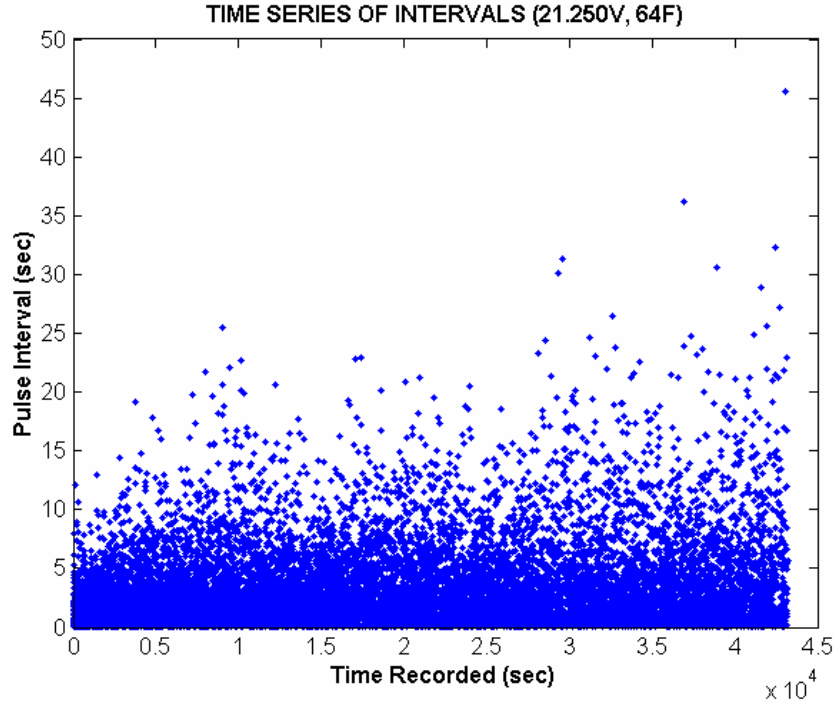
Figure 8.   Plot of time interval between pulse peaks as a function of recording time.

There does not appear to be any sort of periodic behavior. The inter-pulse time intervals appear to vary randomly from pulse to pulse.
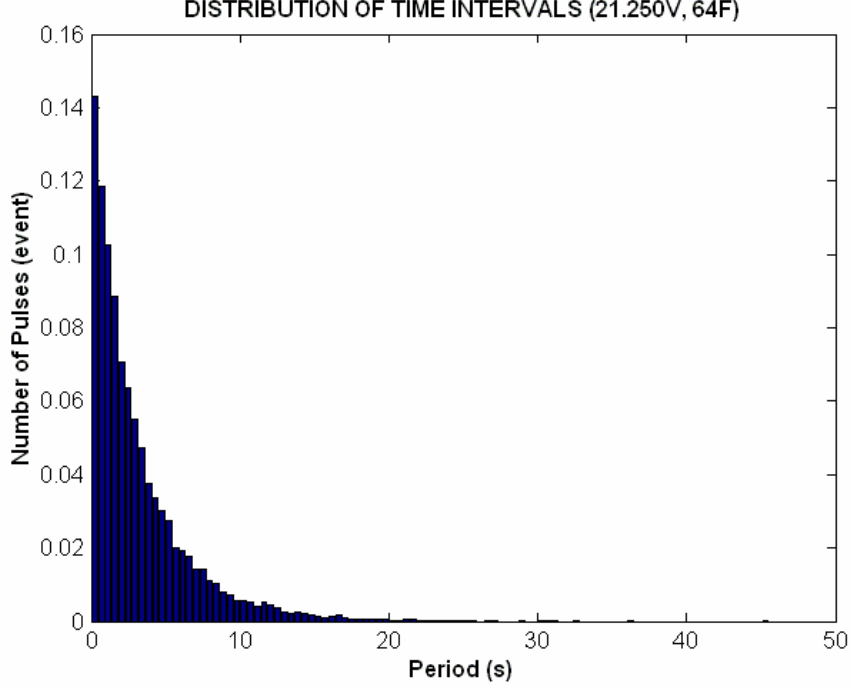
Figure 9.   Histogram of inter-pulse time interval distribution.

Figure 9 is a typical time interval distribution for a series represented by a histogram. The distribution is divided into 100 equally wide bins and the height denotes the number of counts in that bin. The histogram is normalized so that sum of the heights is unity.

The average time interval of the distribution was observed to have an exponential dependence on both the bias voltage and the inverse of temperature as given by the empirical equation 1.2 as:

$$\langle t \rangle = t_0 e^{-\frac{e(V_{SBS} - V_{SBS,T})}{nkT}} \tag{2.1}$$

A.   MEAN TIME INTERVAL DEPENDENCE ON BIAS

The dependence of mean time interval on the DC bias can be understood by analyzing the dynamics of the circuit. The voltage across the SBS is given by

$$V_{SBS} = V_{DC} - V_R \tag{2.2}$$

The voltage across the resistor is a function of time and depends on the RC time constant of the circuit and the voltage across the resistor during the steady state ON condition of the SBS:

$$V_R = V_P e^{-\frac{t}{RC}}$$ (2.3)

The time t is the mean pulse interval for the applied bias. The voltage V_P is the peak value of the voltage across the resistor, as seen in Figure 5. The voltage across the SBS can be written using Equations 2.2 and 2.3 as follows:

$$V_{SBS} = V_{DC} - V_P e^{-\frac{t}{RC}} = V_{DC} - V_P e^{-\frac{1}{fRC}}$$ (2.4)

where f is the mean firing rate which is the inverse of the mean time interval t.

The mean frequency was observed to have the following dependence on bias [1]:

$$f = f_0 e^{\frac{qV_{SBS}}{\eta kT}}$$ (2.5)

The parameter f_0 in Equation 2.5 has absorbed the threshold term in Equation 1.1. The mean time interval is simply the inverse of frequency:

$$t = t_0 e^{-\frac{qV_{SBS}}{\eta kT}}$$ (2.6)

We can rewrite this using Equation 2.4:

$$t = t_0 e^{-\frac{q\left[V_{DC} - V_P e^{-\frac{t}{RC}}\right]}{\eta kT}}$$ (2.7)

This is a transcendental equation for t.

Since at longer mean time intervals or at low bias, the exponential containing RC in Equation 2.7 is negligibly compared to VDC and t_0 can be found using the data in non-saturation region. Figure 10 shows the mean time dependence on bias voltage. It is observed that at the non-saturation condition, the bias voltage is at a minimum when the mean pulse interval time t is equal to 0.69 s.
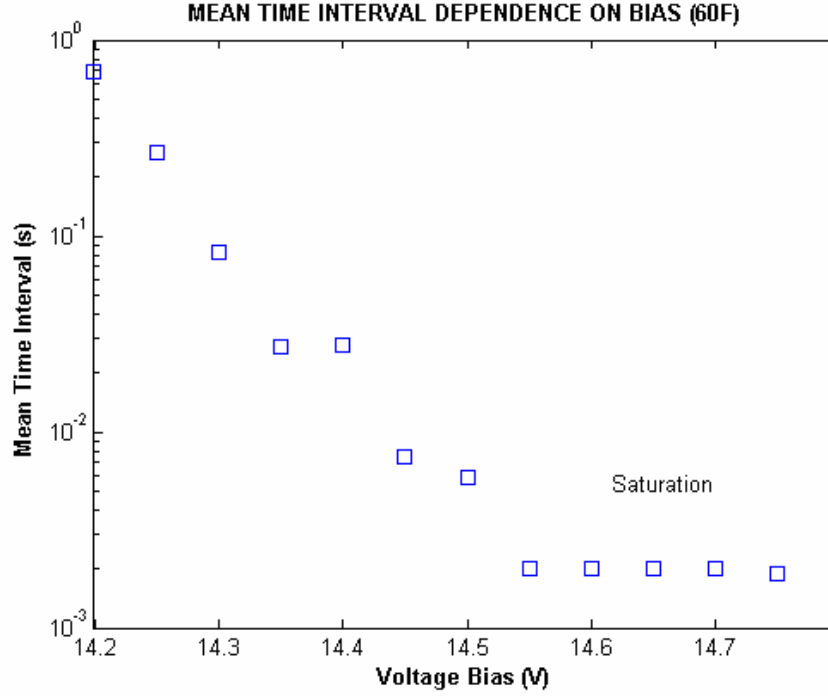
Figure 10.   Saturation occurs as the voltage bias approaches 14.75V

At the non-saturation condition of V_{DC} = 14.20 V and $t_{constraint}$ = 0.69 s and using Equation 2.7 with η = 2, the t_0 can be determined as follows:

$$t_0 = t_{constraint} e^{\frac{q\left[V_{DC_{constraint}} - V_P e^{-\frac{t_{constraint}}{RC}}\right]}{\eta kT}} \qquad (2.8)$$

Using Equation 2.8, we can now find the value of t that solves Equation 2.7 for a given applied bias.

The exponential term contained within another exponential term makes this equation very sensitive to the value of V_P. Thus the dependence of V_P as a function of applied DC bias was measured and the result is shown in Figure 11.
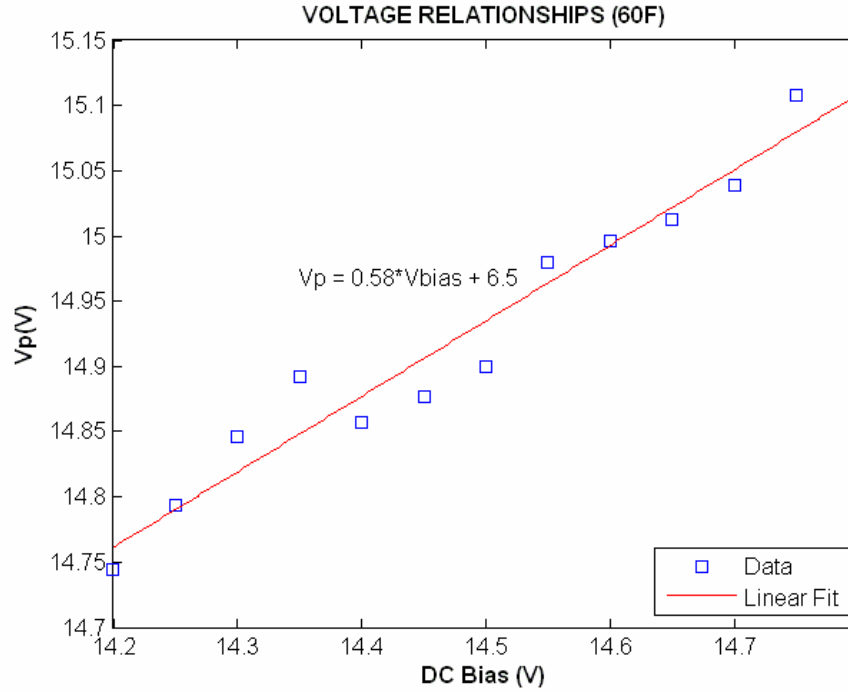
Figure 11.　V_P varies linearly with VDC.

The linear slope equation shown in Figure 11 was used to compute the values of V_P for the fit. These smoothed out values were substituted into Equation 2.7 to get a filtered picture of the dependence of the mean time interval on the voltage bias.

The fit must be calculated by using an iterative approach. By solving the transcendental equation, Equation 2.7, using a loop that tries to get an exact value for the predicted mean time interval for a given voltage bias, we can see that the fitting function provides a very good qualitative match to the data. Figure 12 shows the results of this approach.
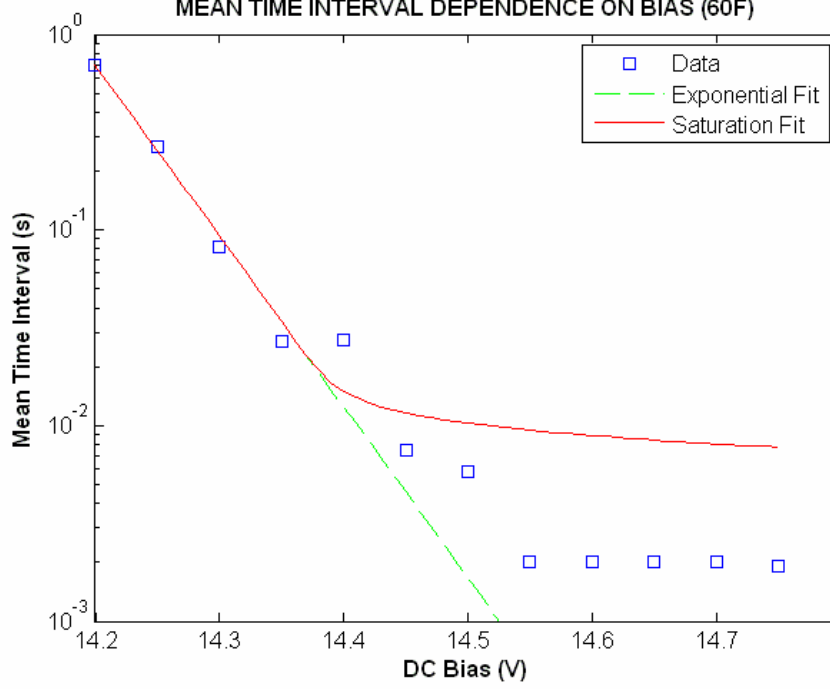
Figure 12. Iterative approach to finding the solution to Equation 2.7. The green dashed line shows the fit with $V_P=0$ in Equation 2.7, which shows the exponential dependence of the mean time interval on bias without the saturation condition imposed. The red line shows the effect of the RC constraint that leads to the saturation condition.

The transition behavior of the iterative solution matches observations for other data sets. Qualitatively, the transitioning between aperiodic and periodic regimes can be understood by applying the maximum firing rate constraints of the RC circuit to the switching mechanism of the SBS, which is best described by PN Hook Theory.

B.   MEAN TIME INTERVAL DEPENDENCE ON TEMPERATURE

The frequency parameter f_0 in Equation 2.5 is proportional to the diode saturation current I_0 from the standard diode equation [1]. I_0 is a function of temperature because it depends upon the carrier concentration directly and this minority-carrier concentration depends on temperature exponentially. If we stay well within the extrinsic range, the value of I_0 can be compared to I_0 at some reference temperature T_0 as follows [5]:

$$\frac{I_0(T)}{I_0(T_0)} = \left(\frac{T}{T_0}\right)^3 e^{\left[-\frac{E_g}{k}\left(\frac{1}{T}-\frac{1}{T_0}\right)\right]} \tag{2.9}$$

16

The diode saturation current I_0 is approximately exponentially dependent on temperature. This qualitative relationship can be seen in the manufacturer data sheet for the MBS4991 Silicon Bilateral Switch produced by Motorolla [3]. Figure 13 shows this relationship.

FIGURE 2 – SWITCHING CURRENT versus TEMPERATURE
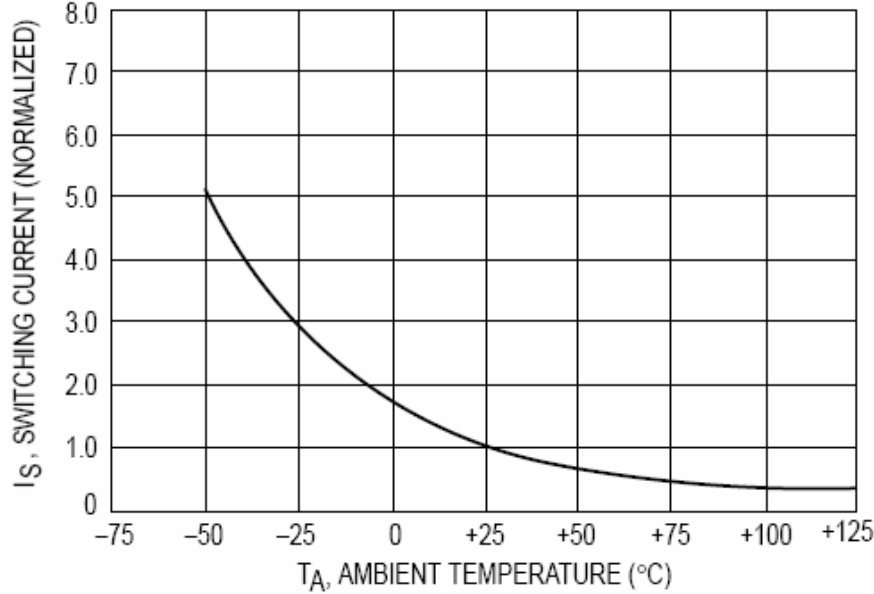
Figure 13.   (Taken from Ref. [3]) Switching current vs. temperature plot from the Motorolla MBS4991 SBS Data Sheet. The current is approximately exponentially dependent on temperature.

This relationship can be used to define a t_0 in Equation 2.7 that is a function of temperature:

$$t_0(T) = t_0(T_0)\left(\frac{T_0}{T}\right)^3 e^{-\frac{E_g}{\eta k T_0}\left(1 - \frac{T_0}{T}\right)} \tag{2.10}$$

where $t_0(T_0)$ is a parameter that represents the saturation time interval for the reference temperature T_0. Note that $E_g \approx 1.66 \times 10^{-19} J$ in Equation 2.16 is the bandgap energy between the conduction and valence bands of the PN diode outer regions [5].

17

The switching voltage has very little sensitivity to temperature, as experimentally observed from Figure 7. This qualitative relationship can be seen in the manufacturer data sheet for the MBS4991 Silicon Bilateral Switch produced by Motorolla [3]. Figure 14 shows this relationship.

FIGURE 1 – SWITCHING VOLTAGE versus TEMPERATURE
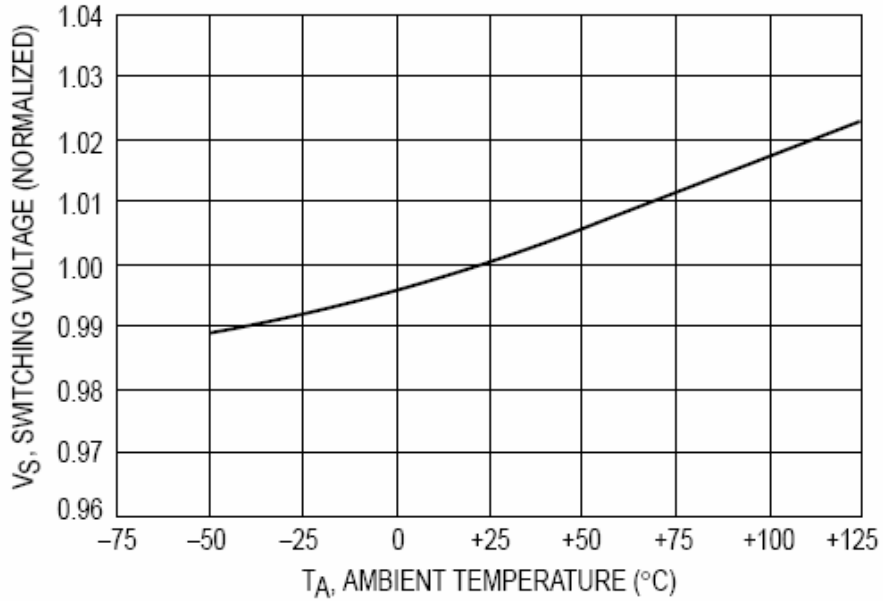
Figure 14.   (Taken from Ref. [3]) Switching current vs. temperature plot from the Motorolla MBS4991 SBS Data Sheet. The switching voltage is weakly dependent on temperature compared to the switching current.

The parameter t_0 is proportional to the inverse of the diode injection current from the outer forward biased PN regions and thus has an effect on the rate at which the thyristor switches on due to filling of the potential wells in the PN Hook model. We can now rewrite Equation 2.7 to include temperature the effects to injection current given by Equation 2.10:

$$t = t_0 \left(\frac{T_0}{T}\right)^3 e^{\frac{E_g}{\eta k T_0}\left(1 - \frac{T}{T_0}\right)} e^{-\frac{q}{\eta k T}\left[V_{DC} - V_P e^{-\frac{t}{RC}}\right]} \tag{2.11}$$

The diode ideality factor η is also weakly dependent on temperature. There are too many unknown variables to provide good fit, but Equation 2.11 gives us a good

18

qualitative description of the behavior. Figure 15 shows the actual mean time interval data. Each color represents a different temperature.
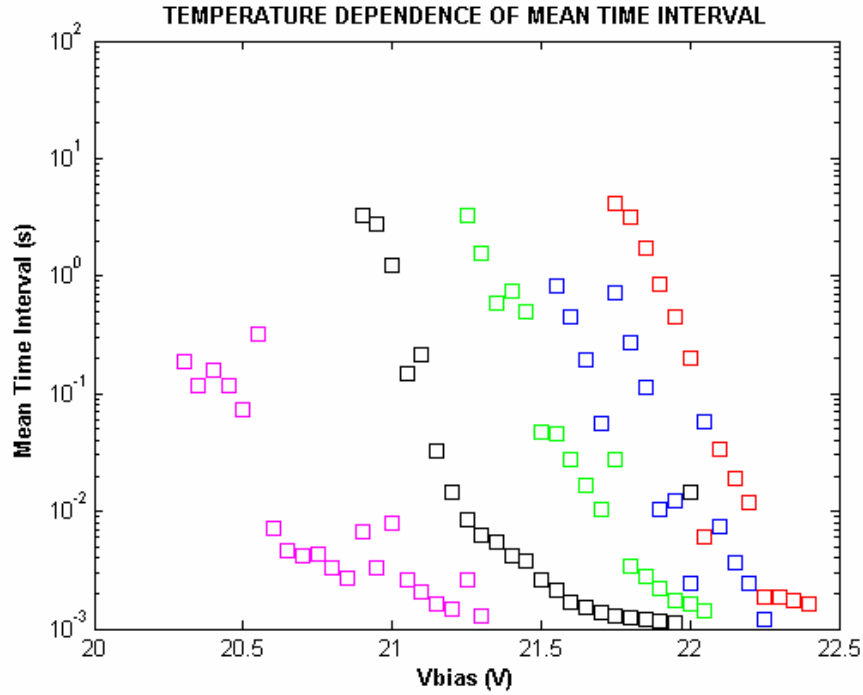
Figure 15.   Mean time interval as a function of temperature. Each color is a
different temperature and each data point represents a different bias.

It is clear from the data that an increase in temperature greatly lowers the required switching current, as shown in Figure 13. It also slightly lowers the switching voltage required to turn on, as shown in Figure 14. This has the effect of shifting the curve left. The slope of the curve also decreases with an increase in temperature, because the mean time interval is exponentially dependent on the inverse of temperature and the ideality factor.

C.   STATISTICAL MODEL

A memoryless process, such as a train of random pulses, depends only on the time of the last event. The probability of when the next pulse occurs depends only on when the last pulse occurs and has no dependence on any of the previous pulses. This behavior can be modeled using a Homogenous Poisson Distribution [6]. Homogenous denotes that the firing rate r is independent of time.

If we consider a total of N pulse spikes in a total time interval T, then the average firing rate is given by $r = \dfrac{N}{T}$. Figure 16 illustrates this example.
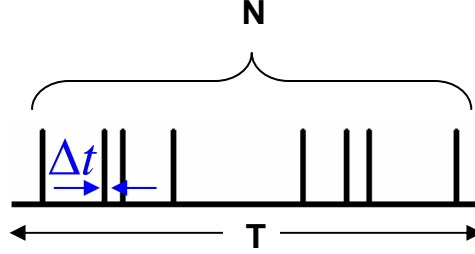
Figure 16.   Time series of spikes.

If the probability that a spike does not occur between time 0 and time t is S(t), then the probability of a spike not occurring in time Δt is S(Δt). The probability of a spike not occurring between time 0 and t+Δt can be written as follows:

$$S(t + \Delta t) = S(t) S(\Delta t) \qquad (2.12)$$

This relation holds true because each event is independent of the other. The probability S(Δt) can be rewritten using the above relationship and a Taylor Expansion of $S(t + \Delta t)$:

$$S(\Delta t) = \frac{S(t + \Delta t)}{S(t)} \approx \frac{S(t) + \dfrac{dS(t)}{dt}\Delta t}{S(t)} = 1 + \frac{\dfrac{dS(t)}{dt}\Delta t}{S(t)} \qquad (2.13)$$

The probability of finding at least one spike within Δt is equal to 1- S(Δt), thus using the result in Equation 2.13, the probability of firing within Δt is given by:

$$1 - S(\Delta t) \approx -\frac{1}{S(t)}\frac{dS(t)}{dt}\Delta t \qquad (2.14)$$

If the firing rate within Δt is equal to the probability of firing in Δt divided by the time interval Δt. If we assume that the firing rate within Δt is independent of time and is equal to the average firing rate r, then the following relationship exists:

$$r = \frac{1 - S(\Delta t)}{\Delta t} \approx -\frac{1}{S(t)}\frac{dS(t)}{dt} \qquad (2.15)$$

20

The firing rate r is a constant, which means that the above differential equation has the solution:

$$S(t) = e^{-rt} \qquad (2.16)$$

This implies that the probability of not having a pulse decreases exponentially with time. The probability of firing for the first time in Δt and not within t can be written as the product of the probability of not firing within t and the probability of firing within Δt :

$$P(t)\Delta t = S(t)(1 - S(\Delta t)) = S(t)\left(1 - \frac{S(t + \Delta t)}{S(t)}\right) = S(t) - \left(S(t) + \frac{dS(t)}{dt}\Delta t\right) = -\frac{dS(t)}{dt}\Delta t \quad (2.17)$$

The probability density P(t) of firing within Δt for the first time is equal to the negative derivative of S(t) which is given in Equation 2.16:

$$P(t) = -\frac{dS(t)}{dt} = re^{-rt} \qquad (2.18)$$

Alternatively, the probability density given in Equation 2.18 can be interpreted as the probability density for having pulse period of t. In other words, it gives the information about the distribution of pulse intervals.

It can be easily shown as follows that having n pulses within a time period T follows the Poisson distribution. If we consider a large time interval T, the probability of just on spike occurring in that interval is a cumulative probability equal to the sum of the probabilities of all the possible times a spike could occur. The probability density of a single spike occurring at t for the first time is given by P(t). The probability that no spikes occur afterwards is equal to S(T-t). Thus, the cumulative probability function $P_T(1)$ that only one spike occurs at any given time within the time interval T is the sum of all probabilities of a spike occurring at precisely the time t and nowhere else:

$$P_T(1) = \int_0^T P(t)S(T - t)dt = \int_0^T re^{-rt}e^{-r(T-t)}dt = rTe^{-rT} \qquad (2.19)$$

Similarly, the probability $P_T(2)$ of two spikes occurring within the time interval T is equal to the cumulative probability of a spike occurring at time t_1, a spike occurring at time $t_2 > t_1$, and a spike not occurring after t_2:

$$P_T(2) = \int_0^T \int_0^T P(t_1)P(t_2 - t_1)S(T - t_2)dt_1 dt_2 = \int_0^T \int_0^T re^{-rt_1}re^{-r(t_2-t_1)}e^{-r(T-t_2)}dt_1 dt_2 = (rT)^2 e^{-rT} \quad (2.20)$$

If we normalize this result for the variable $\lambda = rT$, the probability function must be multiplied by a constant. This can be easily shown by the following integral:

$$\int_0^\infty P_\lambda(2)d\lambda = \int_0^\infty \lambda^2 e^{-\lambda}d\lambda = \left[e^{-\lambda}\left(-\lambda(\lambda+2)-2!\right)\right]_0^\infty = 2! \quad (2.21)$$

For 3 spikes, the normalization constant is 3!, and so on. Thus, the probability of n spikes is the standard Poisson Distribution with respect to λ:

$$P_\lambda(n) = \frac{1}{n!}(\lambda)^n e^{-\lambda} \quad (2.22)$$

1.   Effects of Pulse Width

In our case that the spikes have a width that is greater than zero, the duration of the pulse is known as refractory period in which the probability of the next pulse occurring is zero. This is a behavior commonly observed in neurons [4]. The neuron cannot fire again until it has had time to reset [4]. Figure 17 illustrates the relationship for the inter-pulse wait time $t = \Delta t + t_0$.
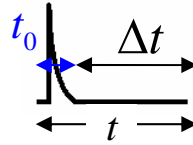
Figure 17.   Inter-pulse time Δt and refractory period t_0.

The effect of pulse width can be taken into account by modifying the function S(t) as follows. Since the probability of not having a pulse during t = 0 and t = t_0, S(t_0), is unity, the probability of not having a pulse between 0 and t can be written as

S(t_0)S(t-t_0) = S(t-t_0). Thus, using Equation 2.18, the probability density of having the first pulse at t can be written as:

$$P(t) = \begin{cases} re^{-r(t-t_0)}, & t > t_0 \\ 0, & t \le t_0 \end{cases} \quad (2.23)$$

In addition, the firing rate needs to be modified to accommodate the pulse width. The firing rate is the total number of spikes divided by the total time interval. Consider the

22

case of a single spike, the firing rate changes from zero during the refractory period to a finite value during the inter-pulse period. The total number of spikes in an interval T can be found by adding the contribution from the refractory period to the contribution from the inter-pulse period. This is equivalent to the number of spikes per inter-pulse period:

$$N = r_{\text{refract}} T_{\text{refract}} + r_{\text{inter}} T_{\text{inter}} = r_{\text{inter}} T_{\text{inter}} \tag{2.24}$$

If we assume $N = 1$, then the average inter-pulse period time is equal to the average time between spikes minus the refractory period:

$$\langle \Delta t \rangle = \langle t - t_0 \rangle = \langle t \rangle - t_0, \quad t > t_0 \tag{2.25}$$

Thus, the firing rate can be defined as follows:

$$r = \begin{cases} r_{\text{inter}} = \dfrac{N}{T_{\text{inter}}} = \dfrac{1}{\langle \Delta t \rangle} = \dfrac{1}{\langle t \rangle - t_0}, & t > t_0 \\[2ex] r_{\text{refract}} = 0, & t \leq t_0 \end{cases} \tag{2.26}$$

Combining the Equations 2.23 and 2.26 the resulting probability density function (PDF) can be obtained as follows:

$$P(t) = \begin{cases} r_{\text{inter}} e^{-r_{\text{inter}}(t-t_0)} = \dfrac{1}{\langle t \rangle - t_0} e^{-\frac{1}{\langle t \rangle - t_0}(t-t_0)}, & t > t_0 \\[2ex] r_{\text{refract}} e^{-r_{\text{refract}}(t-t_0)} = 0, & t \leq t_0 \end{cases} \tag{2.27}$$

This PDF is properly normalized, as can be seen by the following integration:

$$\int_{t_0}^{\infty} P(t)\, dt = \int_{t_o}^{\infty} \frac{e^{\frac{t_0}{\langle t \rangle - t_0}}}{\langle t \rangle - t_0} e^{-\frac{t}{\langle t \rangle - t_0}}\, dt = \frac{e^{\frac{t_0}{\langle t \rangle - t_0}}}{\langle t \rangle - t_0} \left[-(\langle t \rangle - t_0) e^{-\frac{t}{\langle t \rangle - t_0}} \right]_{t_0}^{\infty} = e^{\frac{t_0}{\langle t \rangle - t_0}} \left[-e^{-\frac{t}{\langle t \rangle - t_0}} \right] = 1 \tag{2.28}$$

2. Mean Interpulse Time Interval and Variance

The mean time interval between events can be obtained using the probability density function given in Equation 2.27 as follows:

$$\bar{t} = \int_0^\infty tP(t)dt = \int_{t_0}^\infty rte^{-r(t-t_0)}dt = \frac{e^{rt_0}}{r}\int_{rt_0}^\infty xe^{-x}dx = -\frac{e^{rt_0}}{r}\int_{rt_0}^\infty xd\left(e^{-x}\right)$$

$$\bar{t} = -\frac{e^{rt_0}}{r}\left(\left[xe^{-x}\right]_{rt_0}^\infty - \int_{rt_0}^\infty e^{-x}dx\right) = -\frac{e^{rt_0}}{r}\left(-rt_0e^{-rt_0} - \left[-e^{-x}\right]_{rt_0}^\infty\right) = t_0 + \frac{1}{r}$$

$$\bar{t} = t_0 + \left(\langle t\rangle - t_0\right) = \langle t\rangle, \quad t > t_0 \tag{2.29}$$

It can be seen that as the pulse rate increases, the average pulse interval reaches the refractory period t_0 as expected.

The variance of the interpulse time intervals can be derived as follows:

$$\overline{t^2} = \int_0^\infty t^2 P(t)dt = \int_{t_0}^\infty rt^2 e^{-r(t-t_0)}dt = \frac{e^{rt_0}}{r^2}\int_{rt_0}^\infty x^2 e^{-x}dx = -\frac{e^{rt_0}}{r^2}\int_{rt_0}^\infty x^2 d\left(e^{-x}\right)$$

$$\overline{t^2} = -\frac{e^{rt_0}}{r^2}\left(\left[x^2 e^{-x}\right]_{rt_0}^\infty - 2\int_{rt_0}^\infty xe^{-x}dx\right) = -\frac{e^{rt_0}}{r^2}\left(-\left(rt_0\right)^2 e^{-rt_0} - 2\left[-rt_0 e^{-rt_0} - e^{-rt_0}\right]\right)$$

$$\overline{t^2} = t_0^2 + 2t_0\left(\langle t\rangle - t_0\right) + 2\left(\langle t\rangle - t_0\right)^2$$

$$\sigma_t^2 = \overline{t^2} - \bar{t}^2 = t_0^2 + 2t_0\left(\langle t\rangle - t_0\right) + 2\left(\langle t\rangle - t_0\right)^2 - \langle t\rangle^2 = \left(\langle t\rangle - t_0\right)^2, \quad t > t_0 \tag{2.30}$$

Thus, the expected result is $\sigma_t = \langle t\rangle - t_0$ for a Poisson Process with a refractory period. This is a key characteristic of a Homogenous Poisson Process.

D.   TIME INTERVAL DISTRIBUTION

The average time interval was observed to be time-independent. This was determined by comparing mean interpulse time intervals for different sample sizes from the same series. The number of data points in the sample varied from 1000 to 65536. The estimated average interpulse time interval did not change as the number of data points increased. This is one of the requirements for a *Homogenous* Poisson Process.

The time interval distribution was observed to have the following PDF:

$$P(t) = \begin{cases} \dfrac{e^{\frac{t_0}{\langle t\rangle - t_0}}}{\langle t\rangle - t_0}e^{\frac{-t}{\langle t\rangle - t_0}}, & t > t_0 \\[2mm] 0, & t \le t_0 \end{cases} \tag{2.31}$$

24

The t_0 used was the observed minimum of each data series and in all cases was equal to the refractory period of 1.0 ms which is the RC time constant of the circuit given by Equation 2.7.

1.   Mean

The <t> used in the PDF fit was the observed mean interpulse time $\bar{t}$ of each data series. This is another key characteristic of a Homogenous Poisson Process. Figures 18-25 are plots of the PDF fit to data for temperatures 60 F and 68 F for a set of bias voltages. It is important to note that the fit is especially well suited to describe the behavior of the circuit just prior to saturation.
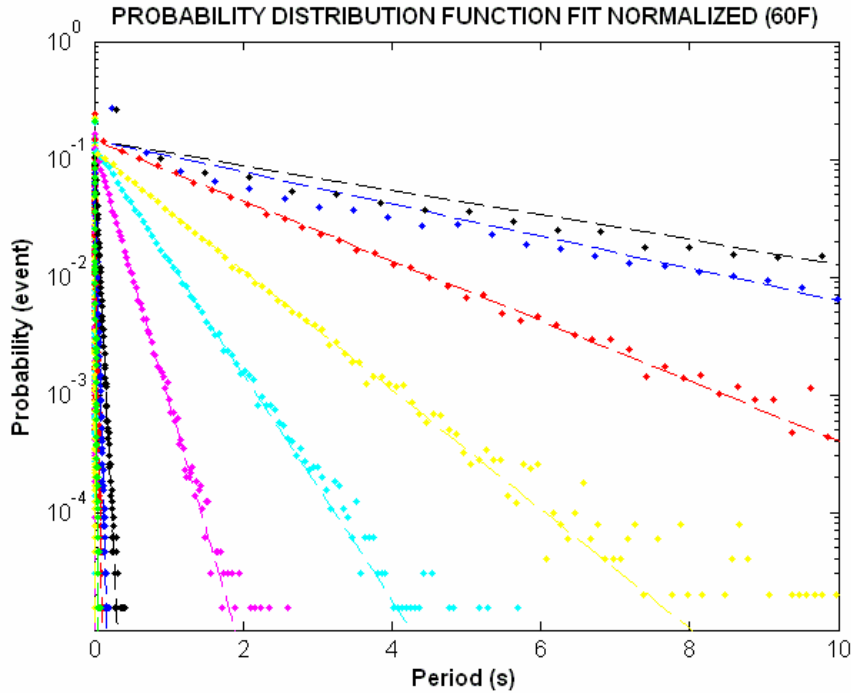
Figure 18.   PDF fit for 60F showing very long time interval (0-10 s) distributions for a set of bias voltages.
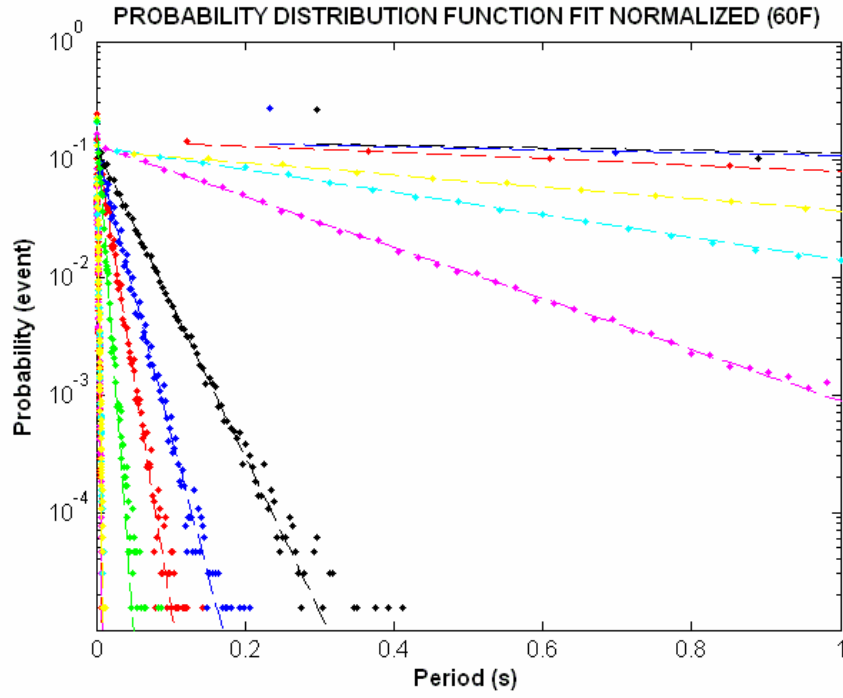
Figure 19.   PDF fit for 60F showing long time interval (0-1 s) distributions.
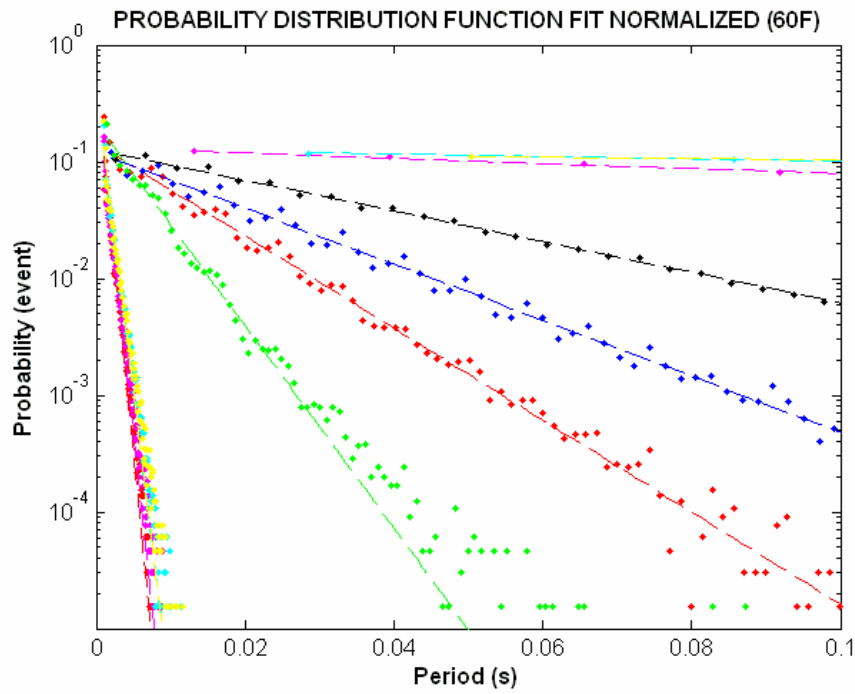
Figure 20.   PDF fit for 60F showing short time interval (0-0.1 s) distributions.
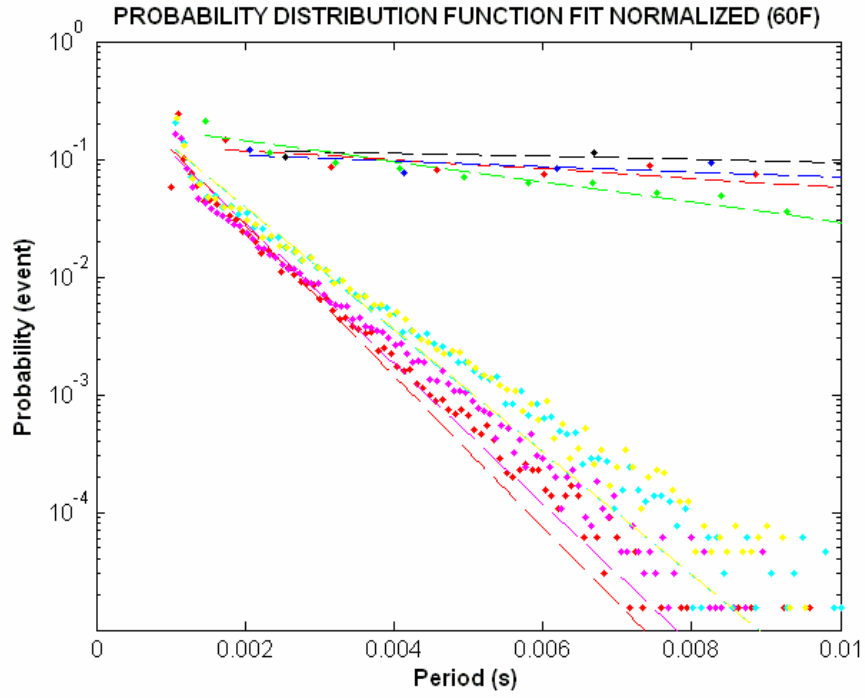
Figure 21.   PDF fit for 60F showing very short time interval (0-0.01 s) distributions.
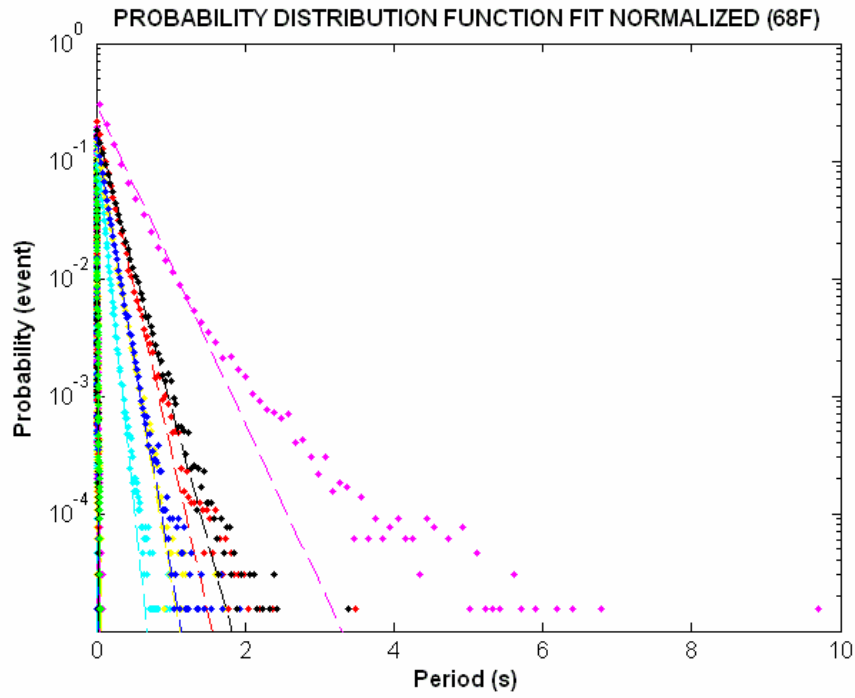
Figure 22.   PDF fit for 68F showing very long time interval distributions.
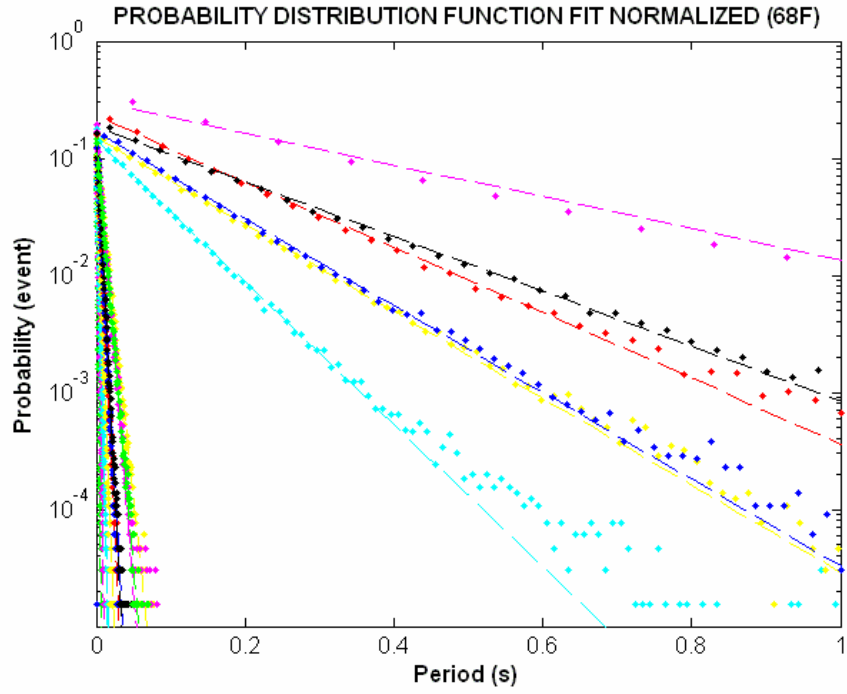
Figure 23.   PDF fit for 68F showing long time interval distributions.
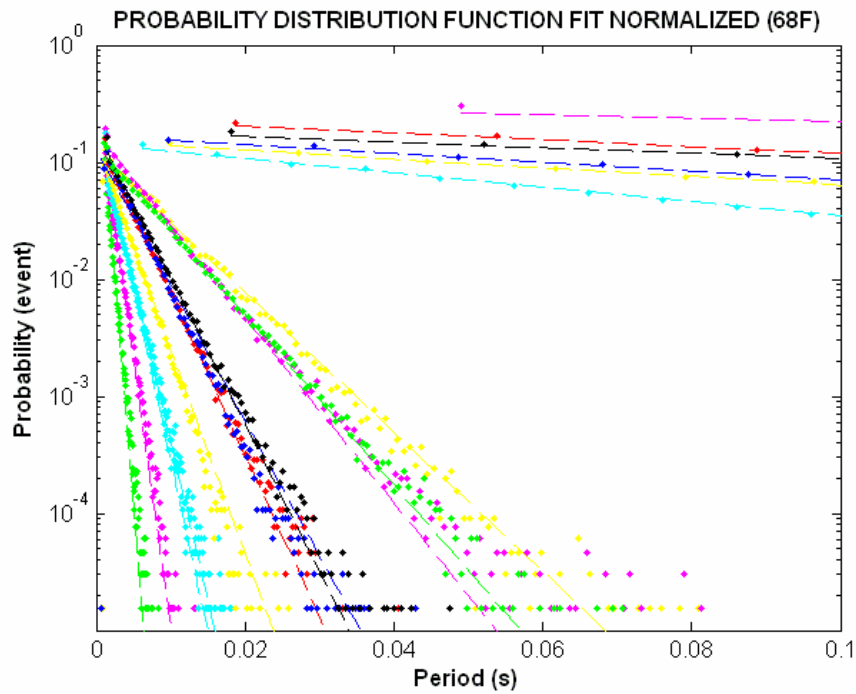
Figure 24.   PDF fit for 68F showing short time interval distributions.

28
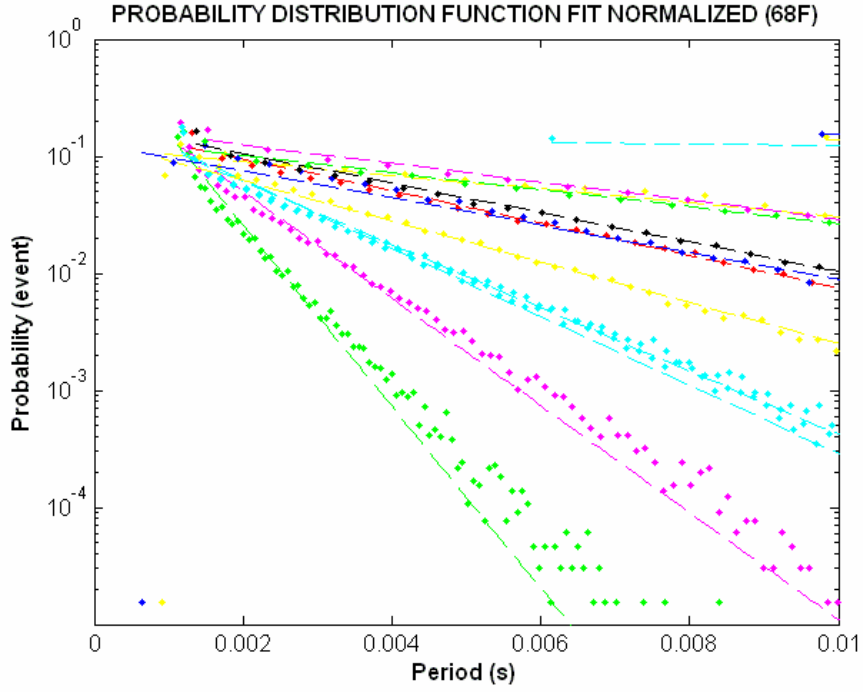
Figure 25.   PDF fit for 68F showing very short time interval distributions.

The PDF fit is an excellent fit for all of the voltage and temperature series collected. This suggests that the pulse generation is a spontaneous, memoryless process described by the Poisson Point Distribution with a refractory period.

2.   Variance

The variance was computed from the data and found to satisfy the following relationship:

$$\sigma_t^2 = \frac{1}{r^2} = \left(\langle t \rangle - t_0\right)^2 \tag{2.32}$$

Figure 26 shows a comparison of the expected σ_t^2 to the actual σ_t^2 for one temperature set.
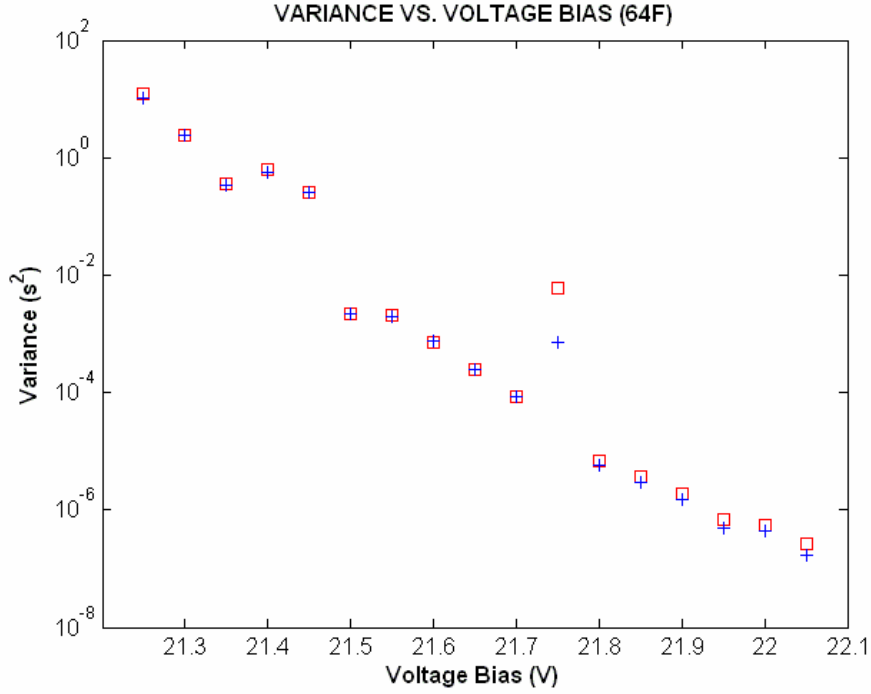
Figure 26.   Comparison of actual σ_t^2 (blue) to expected σ_t^2 (red) using Equation 2.41 for a constant temperature of 64F.

The blue crosses are the data and the red squares are the fit. The fit appears to be very good. The results are the same for the other four temperature sets. This is the final confirming evidence that the pulse generation is a Poisson Process with a refractory period. The key idea is that it is a completely random process where the probability of a pulse occurring depends only the firing rate and the time of the last pulse.

E.   CHAOS ANALYSIS

The time interval distribution of the pulse generating circuit is characterized by a Poisson Point Process with a refractory period. This is a memoryless process in which the generation of a pulse is completely random. There are two sates, ON and OFF, that depend on the external voltage bias and the temperature. The language of Chaos is helpful in further characterizing the behavior of the circuit

30

1.   Power Spectral Density

The most widely used analytical tool is the power spectral density. MATLAB has an easy to use power spectral density tool called the Periodogram Power Spectral Density Tool [7]. This computes the Discrete Fourier Transform of the signal

$$X[f_k] = \sum_{n=0}^{N-1} x[n] e^{-\frac{2\pi jkn}{N}}$$

(2.33)

where x[n] is the voltage waveform in time coordinates and

$$f_k = \frac{kf_s}{N}, \quad k = 0,1,...,N-1$$

(2.34)

is the vector of frequency coordinates. The frequency f_s is the sampling frequency an N is the total number of data points. The Fourier Transform is squared and normalized to get the resulting Power Spectral Density:

$$P[f_k] = \frac{|X[f_k]|^2}{Nf_s}$$

(2.35)

Figure 27 is a Power Spectral Density for periodic (22.40 V, 60 F) and aperiodic (21.75 V, 60 F) pulsing circuits. The sampling frequency is assumed to be 1 kHz and the total time interval is 10 s. This corresponds to 10000 data points and a Nyquist Frequency of 500 Hz. The voltage waveform was reconstructed from the time series of pulse interval lengths by assuming that the pulse firing event (rise time) occurs within 80 ns and therefore the maximum voltage falls into just one of the time bins. All of the other bins are set to the off state voltage, given by the experimental data. This is a bit artificial, but still demonstrates the difference in the frequency components of the firing rate for the two different operating regimes.

31
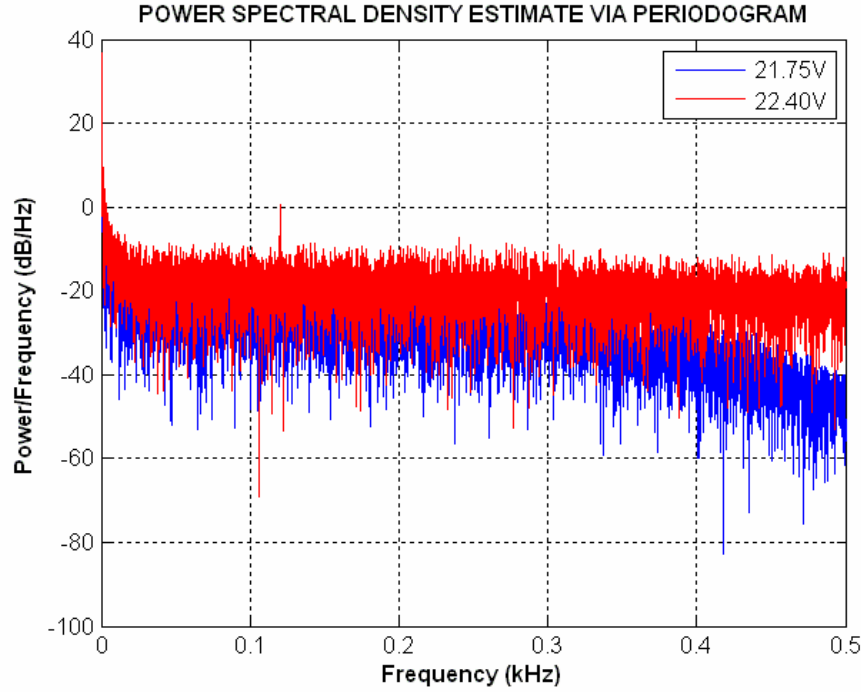
Figure 27.   Power Spectral Density via Periodogram for periodic pulse rate (22.40 V, 60 F, red line) and aperiodic (21.75 V, 60 F, blue line) pulse rate series. The firing rate of the periodic series has more high frequency components, as expected.

The power spectrum can be smoothed by an averaging function. This is usually done by windowing the data into a small segment, averaging what is inside the window, and then sliding the window across the entire spectrum. The windowing in a Welch estimate is done using a Hamming window over n = 8 data points [7]. The Hamming window is defined as

$$\omega(k) = 0.54 - 0.46\cos\left(\frac{2\pi k}{n-1}\right), \quad k = 0,1,...,n-1 \qquad (2.36)$$

All this window does is suppress the high and low frequency components of the data inside the window for a nice smoothing effect. Figure 28 is a Power Spectral Density estimate via Welch method for the data in Figure 27.

POWER SPECTRAL DENSITY ESTIMATE VIA WELCH
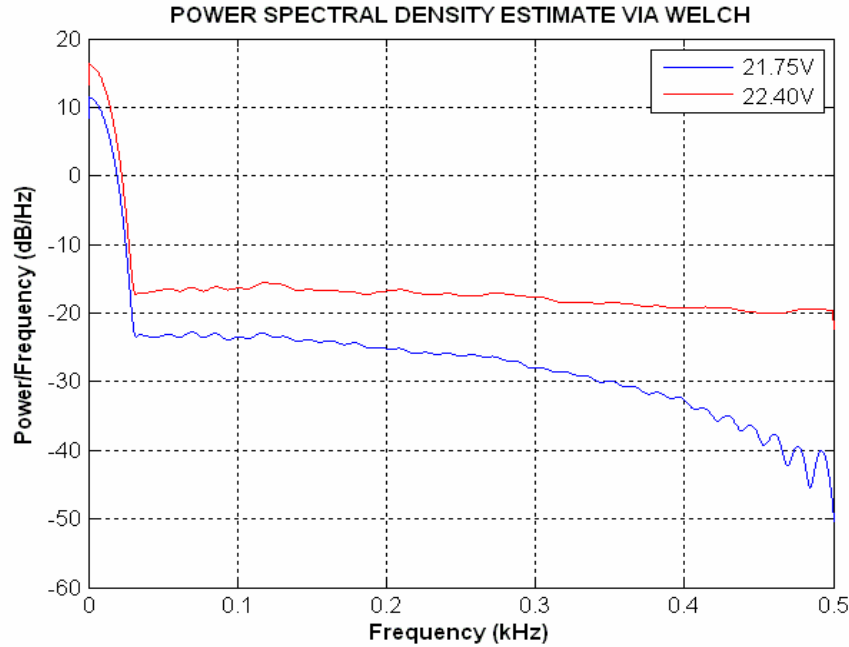
Figure 28.   Power Spectral Density via Welch for periodic pulse rate (22.40 V,
60 F, red line) and aperiodic (21.75 V, 60 F, blue line) pulse rate series.
The firing rate frequency components are the same as in figure 29, but
with a much smoother estimate.

The variance of the long time delay circuit is much larger than the variance of the short time delay circuit, which affects the shape of the spectrums at high frequency. Figures 27 and 28 show the firing frequency of the periodic series (22.40 V) has more high frequency components, as expected. The long time delay represents a less constrained process in which the distribution of firing frequencies corresponds to aperiodic operation. In contrast, the short time delay is a more constrained process, in which the firing rate of the device approaches periodic operation of 1kHz.

2.   Embedding

Embedding is used to detect memory within a process by looking at the dependence of the current value on the previous values. In this technique, a vector of data is shifted by one place and then plotted against itself. Figure 29 is an embedding plot for a circuit operating with a very large average time delay between pulses. Figure 30 is an embedding plot for a circuit operating with a very small average time delay between pulses.
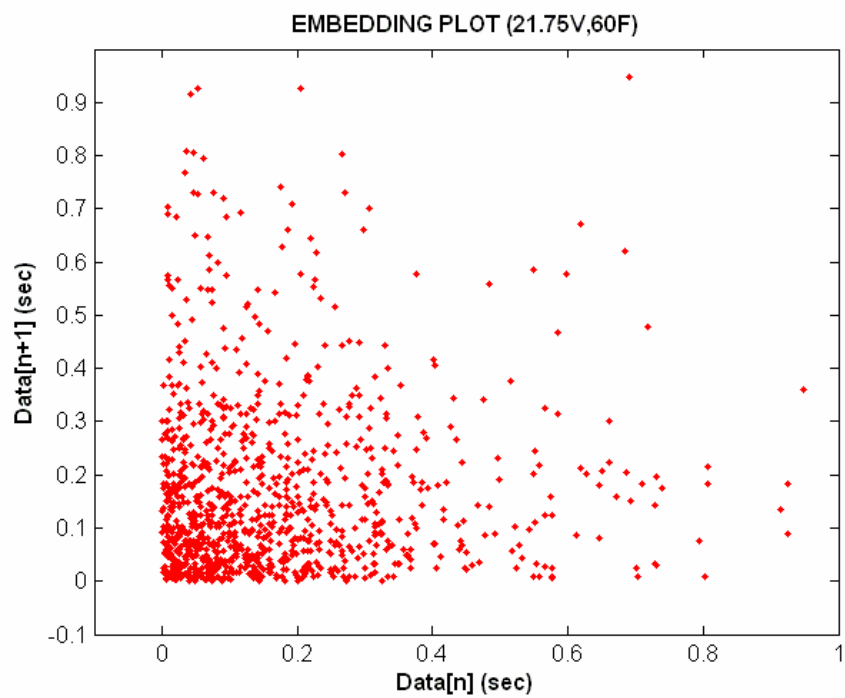
Figure 29.   Embedding of a series characterized by a large mean time interval
<t>.
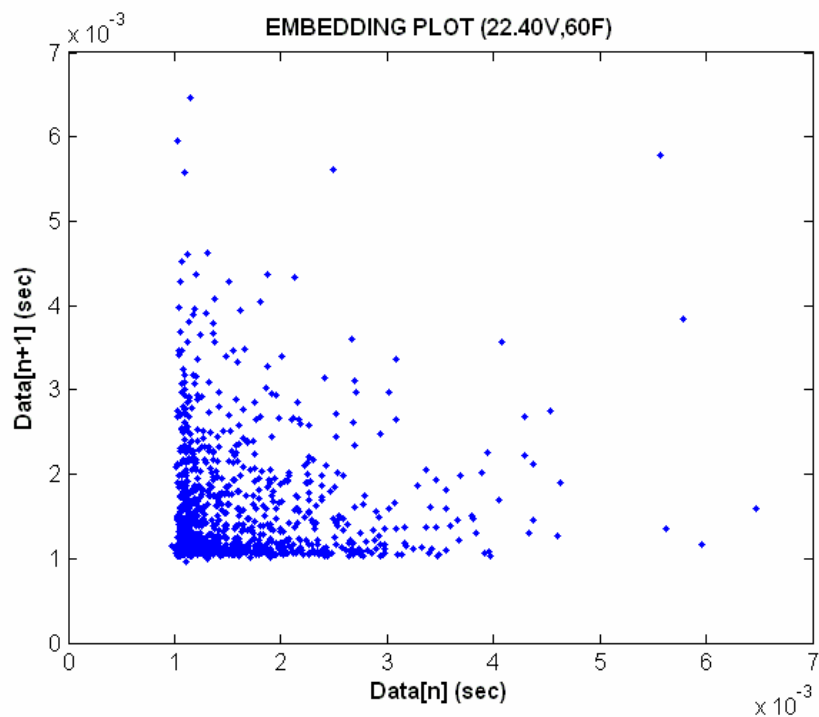
Figure 30.   Embedding of a series characterized by a small mean time interval
<t>.

Both of the embedding plots are highly dispersed. This is confirming evidence that the process is highly memoryless.

A higher order embedding can be used to look for further detail. A plot of a third vector shifted by two against the 2D embedding plot produces a 3D embedding plot. Figure 31 is a 2nd order embedding plot for the large <t> case. Figure 32 is a 2nd order embedding plot for the small <t> case.
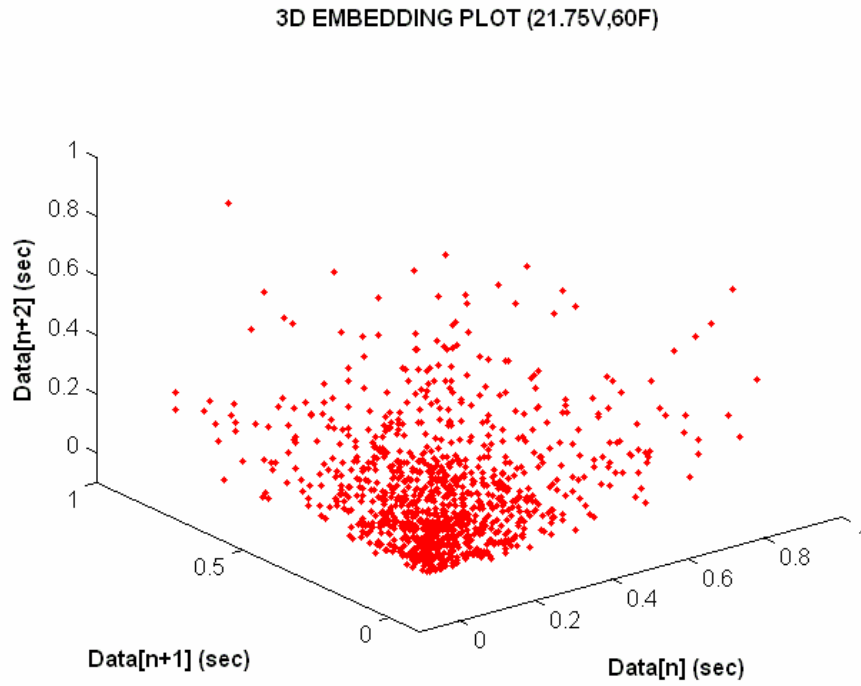
Figure 31.   Large <t> 2nd Order Embedding
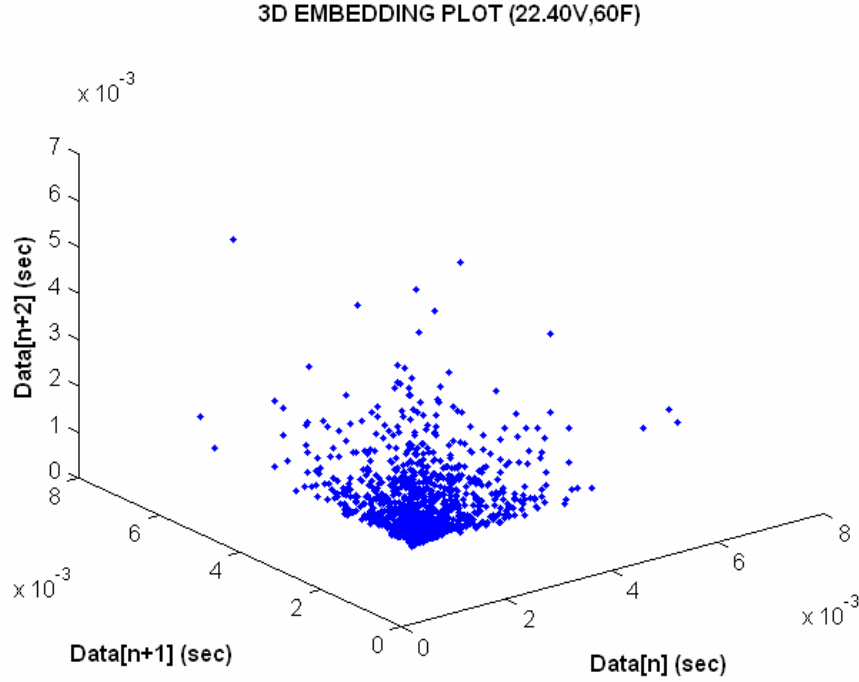
Figure 32.   Small <t> 2nd Order Embedding

Once again, both of the 2nd order embedding plots are highly dispersed. This is further proof that the process is highly memoryless.

3.   Lyapunov Exponent

One of the key characteristics of a chaotic process is sensitivity to initial conditions. The Lyapunov Exponent λ is a measure of the exponential divergence of a system from two very similar starting conditions. It is computed using the following expression [8]:

$$e^{\lambda} = e^{\frac{\Delta t}{\Delta t_0}} \tag{2.37}$$

where Δt_0 is the initial difference in time interval length and Δt is the final difference in the time interval length. For the pulse interval data, two time intervals within 10ms were chosen as start points. The two start points were propagated 20 steps, then the difference between the time intervals located 20 pulses ahead of each initial data point was computed. Figure 33 is a plot of the propagation paths of two different data points for 20 steps.
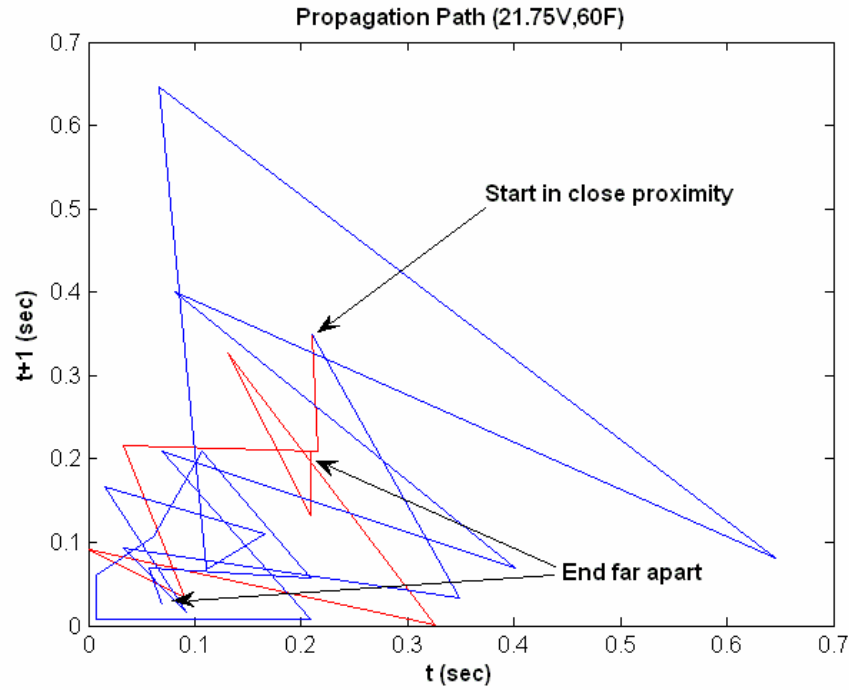
Figure 33.   Two propagation paths for two points that begin close together in
Poincare phase space.

The logarithm of the final difference over the initial difference is the Lyapunov Exponent for that 2 point data set. 20 Lyapunov Exponents were computed at random start points for a data set. The average of the 20 exponents is approximately the average Lyapunov exponent for the entire data series. Figure 34 shows the average Lyapunov Exponent computed for the 60F temperature data set.
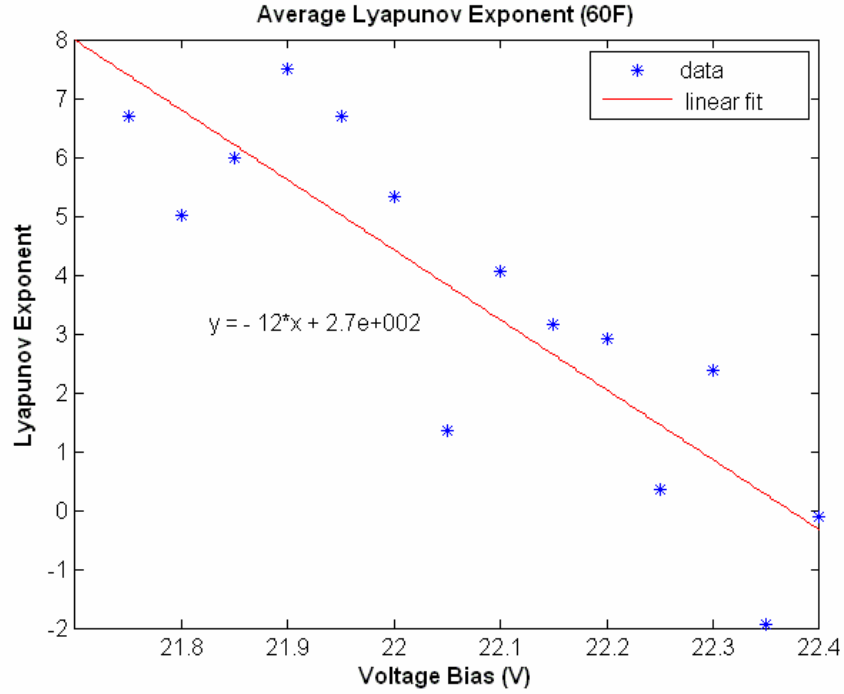
Figure 34.   Average Lyapunov Exponents for 14 different data sets with
different bias at 60F.

The decrease in Lyapunov Exponent corresponds to a decrease in the variance of
the average time interval distribution. This variance depends exponentially on the
temperature and voltage bias. Thus, the aperiodic series are characterized by a strong
sensitivity to initial conditions while the periodic series are characterized by a weak
sensitivity to initial conditions.

4.   Autocorrelation

The Autocorrelation Function is useful to determine whether there are higher
order periodic patterns in a series of data. It is given by the following formula [9]:

$$C(t) = \int c(t+\tau) c(\tau) d\tau \tag{2.38}$$

The integral acts like a sliding window that multiplies the series times a selection of itself
that is shifted along by the window. Figure 35 is a set of correlation plots for an aperiodic
series.
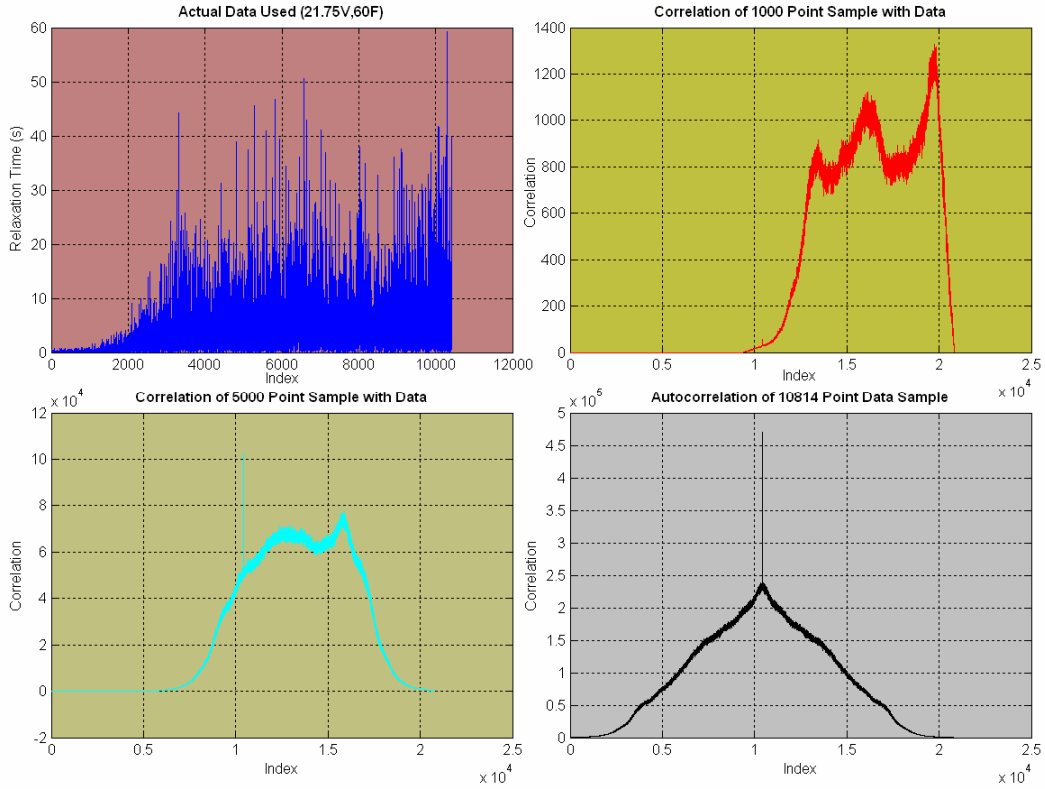
Figure 35.   Correlation plots of various sample sizes with the entire series. The
index is the order in which the data was recorded in the series.

Of particular interest is the autocorrelation in the bottom right plot. The single large spike in the middle represents a perfect correlation, when the shift is zero. The smooth, triangular envelope of the rest of the plot is characteristic of randomness. This is evidence that there are no higher order relationships between pulse intervals.

5. Correlation Dimension

The correlation dimension is a useful tool to look for patterns in a very disperse embedding plot. The data is embedded in a 2D map which creates a trajectory of N-1 points in Poincare phase space. For each point i on the trajectory, the number of points lying within the distance R of the point i are counted, with the exception of i itself. This number is Ni. Next, Pi=Ni/(N-1) is calculated to be the relative number of points within distance R of i. Figure 36 shows a graphical depiction of this counting mechanism.
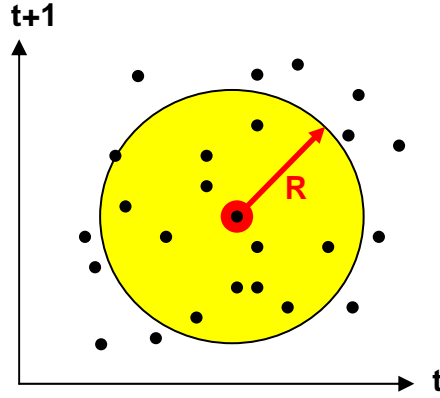
Figure 36.   Counting mechanism.

The correlation sum $C_i = \frac{1}{N}\sum P_i$ is then computed for the space for the given R. The correlation dimension D^C is determined from the slope of the plot of correlation cum vs. R over the "scaling region" [8]. This is the region where R is between the minimum and maximum correlation sums. Figure 37 is a correlation sum plot for an aperiodic series. Figure 38 is the correlation dimension plot for the series in Figure 37. Figure 39 is a correlation dimension plot for a periodic series.
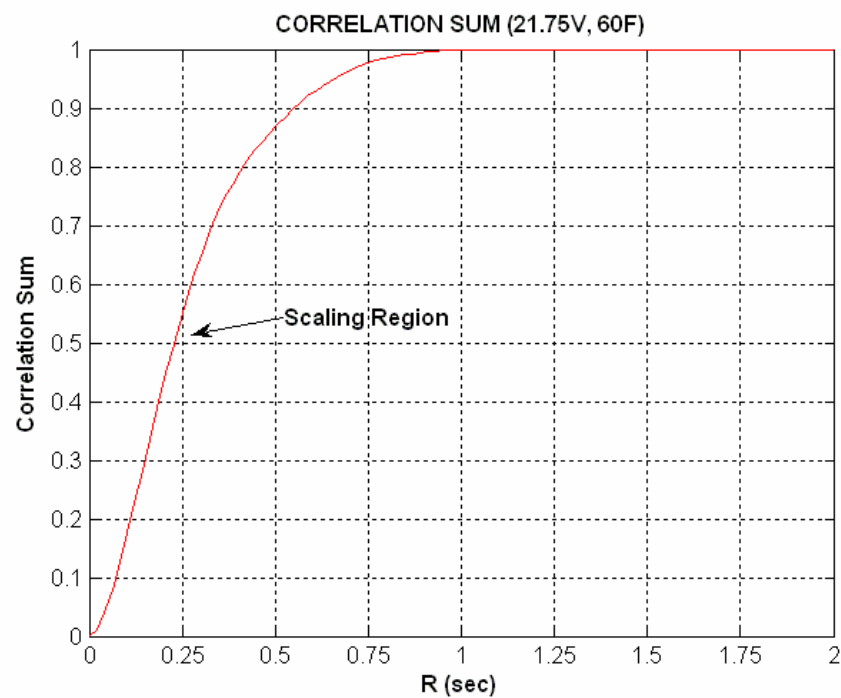
Figure 37.   Correlation sum for an aperiodic series.
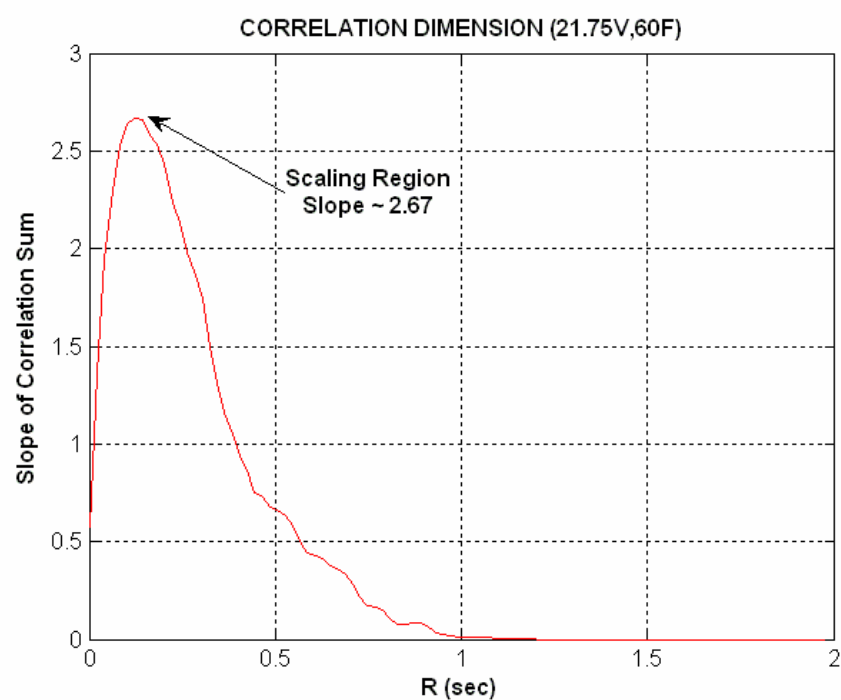
Figure 38.   Correlation dimension for the aperiodic series in Figure 39.
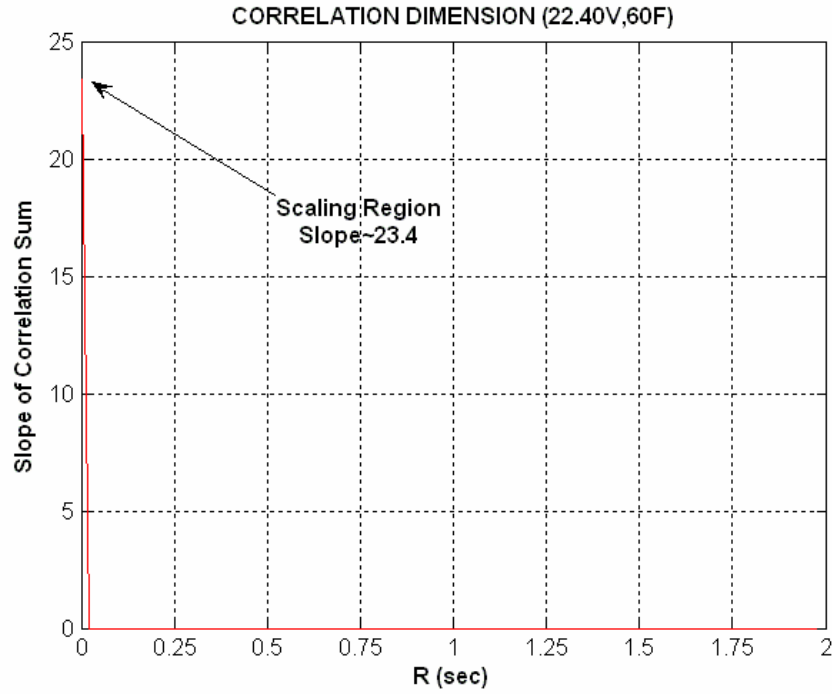
Figure 39.   Correlation dimension for a periodic series.

The scaling region of the correlation sum plot has a smooth, gradually changing slope. This behavior is generally associated with random processes [8]. For both the aperiodic and periodic cases, the correlation dimension reflects the variance of the data.

6.   Conclusion

The conclusion that can be drawn from chaos analysis is that pulse generation is a memoryless process. The temperature and voltage bias set the average firing rate somewhere between the periodic and aperiodic regimes. The pulse interval distribution exhibits a great deal of sensitivity to temperature and voltage bias. This sensitivity to initial conditions is the key defining characteristic of a chaotic system. Pulse generation within the inter-pulse period is observed to be a random process with a time independent firing rate.

III. APPLICATION OF PULSING CIRCUIT

This chapter discusses the usefulness of the circuit to applications involving a distributed processing system capable of swarming. The first goal of this chapter is to show that the ability to transition between chaotic and periodic operating regimes is the key enabler of an emergent behavior swarming model. The second goal is to describe the successful construction of macro-robotic platforms capable of swarming using the SBS circuit studied in Chapter II. Finally, the design of a micro-robotic swarm using standard complementary metal oxide (CMOS), micro electromechanical system (MEMS) and Radioisotope Micro Power Source (RIMS) processes is presented.

A. EMERGENT BEHAVIOR MODEL

In his book Emergence, Steve Johnson defines self-organizing systems as bodies of individual entities whose behavior as individual entities results in a higher level of intelligence to guide that behavior [10]. This higher level of intelligence is unpredictable and is therefore classified as *emergent behavior* [10]. Archetypes in nature include flocking and swarming behavior. For example, a swarm of ants consists of individual units that have a limited piece of the big picture and a rather small instruction set, but act together to forage food, form bridges, construct complex hives and defend territory. The complex behavior that emerges is always unpredictable and is influenced by random events in the environment. This does not deter the ants from reaching their goal. Each ant is part of a distributed processing network that is decentralized and each ant has the same basic capabilities as the rest.

1. Distributed Processing

Swarming and flocking behavior can be modeled by genetic algorithms. John Koza, a consulting professor of computer science at Stanford, is credited as the creator of genetic algorithms which demonstrate emergent behaviors that arise from a distributed processing network [11]. His algorithms are widely used in research and have even been applied to combat simulations. The ISAAC project is one example of this type of combat modeling which was created in 1997 by the Center for Naval Analysis [12]. ISAAC has an impressive set of emergent behaviors that arise from a decentralized force of infantry

and armor units. These behaviors include forward advance, frontal attack, local clustering, penetration, retreat, attack posturing, containment, flanking maneuvers, defensive posturing, "guerilla-like" assaults and encirclement of enemy forces [12]. Of particular interest in the ISAAC model is that a decentralized force may able to evolve its own command and control structure [12]. This means that in the absence of a pre-ordained command and control unit, the force can carry on all of the functions of command and control required to reach its end state.

If this model is applied to warfare, many ideas transcend from the archetypes in nature to next-generation combat forces. *Individual units collect locally available data and act locally.* This is an extremely important concept and is the next step beyond network-centric warfare. The global network that is established with network centric warfare enables real-time control of an entire operation's execution. The data flow on the net can be over-driven, resulting in an "embarrassment of riches" for the operational commander and his staff. Further, the global network can be compromised by the enemy because it is required to operate continuously and individual units must be part of it in order to operate effectively. The emergent behavior model does not require real time command and control over a global network. Individual units only require interaction with their local environment and are collectively able to think and act globally via distributed processing.

2.   Artificial Intelligence

Distributed Processing Systems are highly adaptive and like ISAAC, are capable of learning. The emergence of artificial intelligence is a science fiction term known as *rampancy* in which an AI has limited self-awareness and can adapt like a neural network [13]. In this approach, information operations and cyber warfare are used to disrupt information flow by exploiting a "self-aware" AI to respond to communication actions of the regime. The AI learns to be more effective as it operates. No kinetic force is required, rather the AI adapts to the local information flow and learns how to adapt to the environment and target the regime. The General can't command if he can't communicate. This adaptive learning concept was first realized in 1994 in the cutting edge adaptive AI of the Marathon videogame [14] and can be directly applied to Information Operations in Military Operations Other Than War.

All of the emergent behavior models require an understanding of complex systems capable of distributed processing. The fundamental enabler of a distributed processing system is the ability to transition between random and periodic processes. The capability to rapidly evolve and the speed of operation are key characteristics that make distributed processing systems highly desirable for use in warfare.

3. Swarming

One application of the thyristor pulse-mode logic is that it can be used in a distributed processing network. The ability to transition from chaotic to periodic pulse rate regimes is a key enabler for swarming. In the chaotic pulse state, the output can be used to enable a random walk process. In the periodic pulse state, the output can be used to enable a goal-seeking routine. The transition from random walk to periodic goal seeking is accomplished by application of input bias.

4. Robot Design Concepts

The thyristor circuit demonstrates both chaotic and periodic behavior based on voltage and temperature biasing [15]. Figure 40 shows typical outputs of the logic circuit.
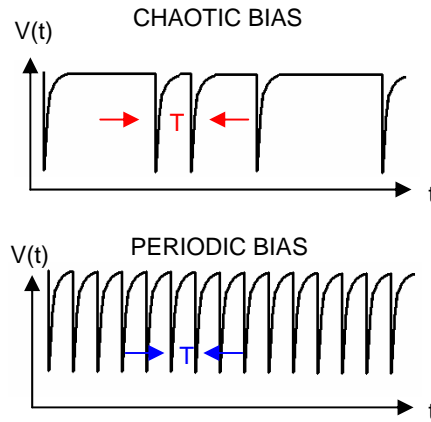
Figure 40. Output voltage is across the thyristor. The thyristor cathode is grounded.

This dual-mode of operation can be used to produce the required logic for a robot to swarm. It accomplishes this by biasing the thyristor circuit based on sensory input. The robot will have a sensor on each side that applies a voltage to the gate of a thyristor circuit used to drive a leg bank on the opposite side. In the absence of light, the leg bank will operate chaotically. In the presence of light, the leg bank will operate periodically

and turn the robot towards the light source. Both leg banks operate independently and the end result is that the robot demonstrates random walk ability and can hunt for the brightest light source.

The swarming robot design also requires an LED in the back of the robot. When other robots see this light source, they turn towards it. This characteristic allows flocking. If the robots can also sense a human IR light source, then the ones closest will turn towards it. The ones behind them will turn towards the ones in front. The ones behind them will turn and so on. The end result is a swarm directed towards the human. Figure 41 shows an example of the sensor logic.
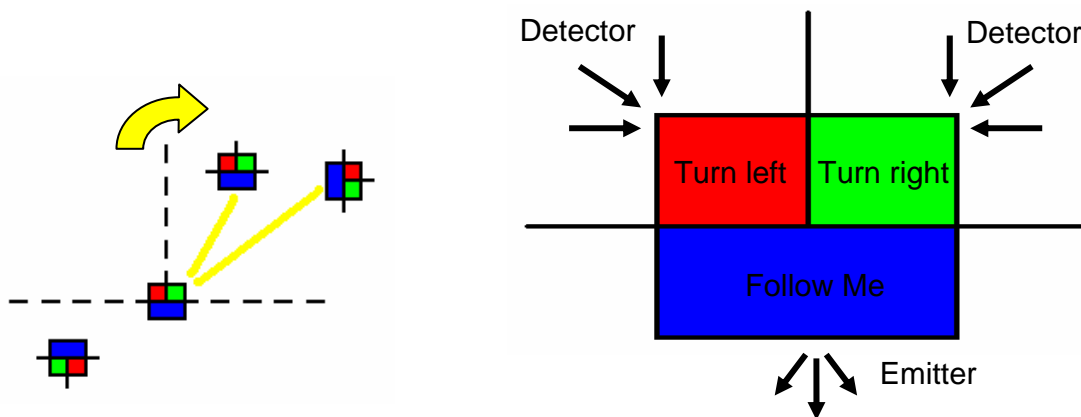
Figure 41.   The left diagram shows the turning effect that incident light has on the robot. The right diagram graphically depicts the sensor and emitter logic.

5.   JAVA Simulation of Swarming Behavior

A simulation of swarming behavior was created using JAVA. Figure 42 shows the GUI that was designed to allow the user to control the swarm. The interface options allow the user to change the size of the swarm and to move the human light source to one of the four corners during the simulation. There is also the option to select one robot and watch its relative picture in the mini-map. This is a North-up view that moves with the robot and keeps track of its closest neighbors. The total intensities on the left and right sensors of the selected robot are tracked by the intensity meter.

46
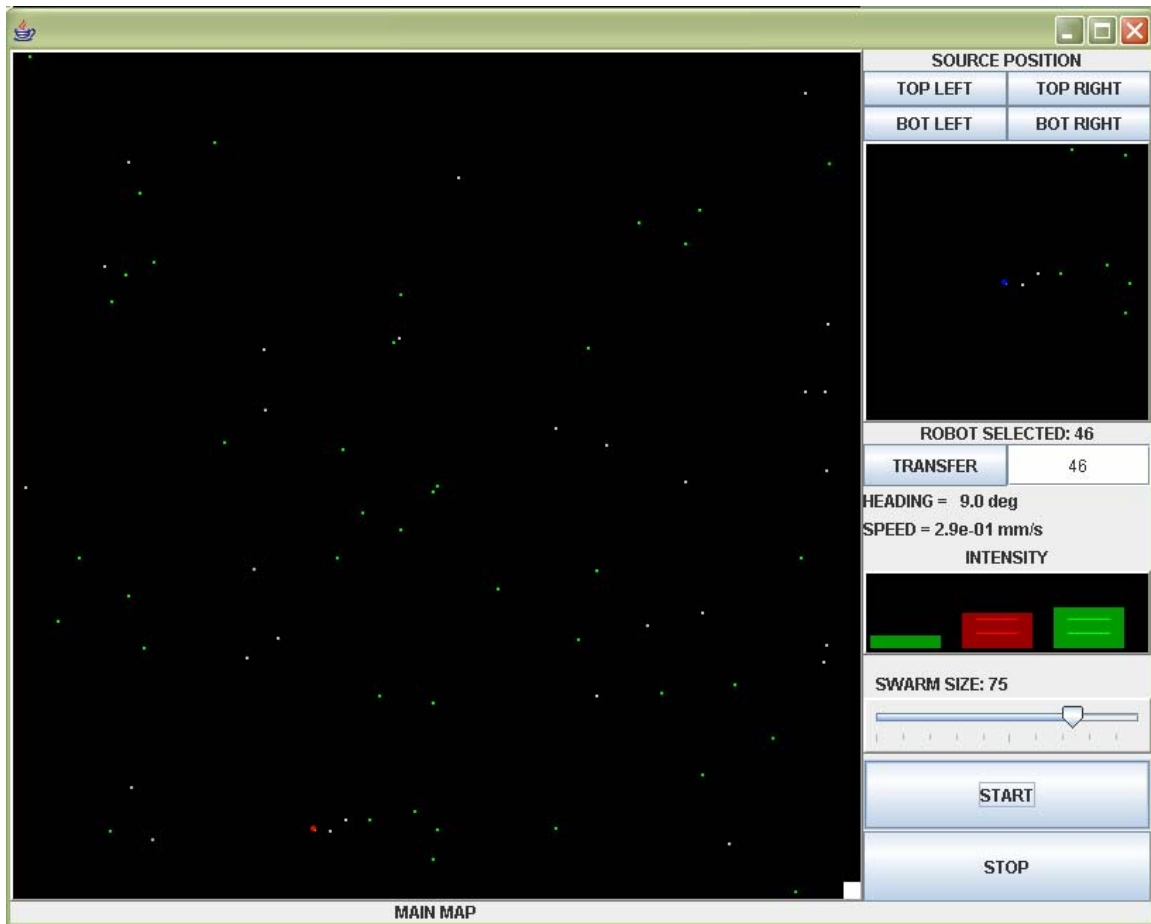
Figure 42.   Graphic User Interface (GUI) for a JAVA based large swarm
simulation program. The green dots are micro-robots and they move
according the physics rules defined in the program. The grey dots are
micro-robots that have landed on their back during the initial deployment
and are therefore unable to move.

This simulation used the First Rayleigh-Sommerfeld solution for incoherent intensity addition on the sensor in order to account for the obliquity of the light sources on the sensor [16]. The robot sensor and emitter layout is identical to the picture in figure 41. It was assumed that the light source was of uniform intensity for 180 degrees. It was desired to model the physics of light propagation and the intensity of the light source was added to the random signal drive power. This linear addition of speed to a random speed signal is an approximation to the actual thyristor logic, but the end result is the same.

The simulation shows that in the absence of a light source, the robots exhibit flocking behavior. It is even possible to get the robots to mill in a circle if the sensor gain

is increased. In the presence of a strong light source, all of the robots turn towards it and close in on it. If the sensor gain is tuned to allow flocking and while avoiding saturation by the strong light source, swarming occurs. The robots closest to the human turn towards it and close in. The robots behind them see the LEDS of the robots in front all leading to the human and turn towards them. The ones behind them turn as well. In seconds, most of the population of robots is speeding towards the human.

The robots not engaged in swarming are looking away for another strong light source. If the light source is moved to another corner, it is these stray robots that are first to detect it, and within seconds the swarming begins anew. This is a demonstrated highly adaptive network.

B.   MACRO-SCALE ROBOT SWARM

The power of the pulse mode thyristor circuit is its scalability. Because only three components are required to produce the logic required for swarming, it is easy to make very simple devices that take advantage of the ability to scale the required circuitry down to a very small footprint. It was this idea that lead to the application of the pulse mode logic technology to micro-robot design.

In order to test the design concepts for a Micro Electro-Mechanical System (MEMS) based micro-robot swarm, a macro-scale model of the swarm was desired. Three robots were constructed from standard electronics components and easily fabricated chasses. Pulse mode logic was successfully evaluated using these models.

1.   Design Considerations

The macro-scale model was designed as proof of concept for the pulse mode logic. Because of this, off-the-shelf components were selected to support the logic and sensing functions. The leg banks were replaced with wheels and DC motors and the power supply was constructed from 9V batteries. The resulting electronic circuits operated as desired, but considerable attention had to be paid to reducing the noise caused by the motors.

2.   Chassis Design

The chassis was constructed from 3mm plastic and 1/32 scale battery operated monster trucks from Tamiya. The electronics were placed in an aluminum project box, and the sensors were mounted externally. Figure 43 shows pictures of the robot.
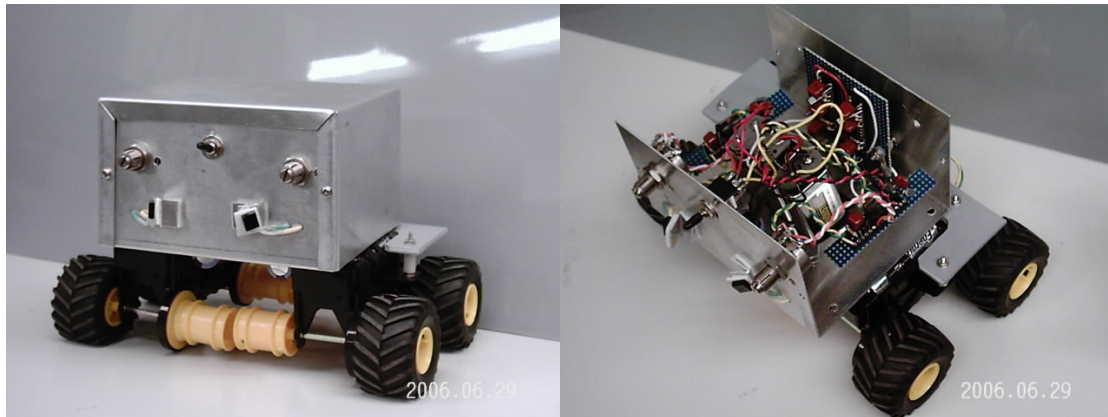
Figure 43.   Robot platform.

The gearing of the toy trucks was such that the device has enough torque to allow a slow random walk signal to easily move the chassis. The big tires allow better grip, an independent power supply for each of the motors reduced the noise and allowed for ease of battery replacement.

The front wheels are free to rotate and the rear tires are independently controlled, which allows for very sharp turns. This is of particular importance in simulating the hunting behavior of the device locking onto a light source and following it.

3.   Electronics Design

The electronics were designed to allow the thyristor circuit to drive a single rear wheel based on an IR sensor input. Figure 46 shows a functional diagram of one side of the electronics.
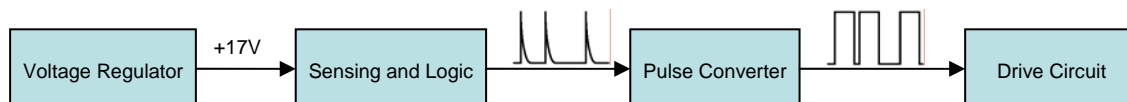
Figure 44.   Robot functional diagram.

The actual schematic of the electronics circuit constructed is found in the appendix. All electronics were hard wired in sockets on perf-board for ease of component replacement.

4. Power Supply

The power supply was reduced in size to three 9V batteries in order to reduce the weight of the vehicle. Because of this, there are many filter components to prevent cross-talk between the left and right sensor circuits. A small resistor was added in series to prevent the thyristors from switching on when the power was switched on.

5. Voltage Regulator

One of the key requirements for operation of the pulse generating circuit is a stable +17VDC bias. This was accomplished by use of a voltage regulator circuit. An externally mounted potentiometer allows manual tuning of the DC bias in order to compensate for ambient light sources and temperature variations. This method of power regulation actually worked quite well and should be considered for more complex micro-robotic designs.

6. Sensing and Logic

This element is at the heart of the design. It consists of a Silicon Bilateral Switch pulse generating circuit and a photo diode connected to the gate of the thyristor. Figure 45 shows the schematic for this element.
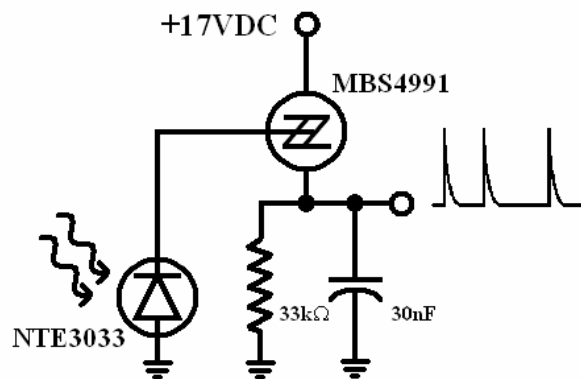
Figure 45.   Sensing and logic.

The photo diode injects current into the gate in proportion to the intensity of the light it detects. This current changes the pulse rate of the circuit. In the absence of light, the circuit pulses chaotically. In the presence of light, the device transitions to periodic

operation. The light could be incident on the thyristor gate itself, but the casing to the thyristor would have to be removed. It was much easier to use a photodiode.

The refractory period is given by RC = 1.0 ms. The success of the sensor and logic circuit is heavily dependent on photodiode selection. The ideal case is a large area photodiode with low dark current and at least 1 mA peak current. It is important to note that this is analog signal processing. It is very fast and requires only four components. The downside is that it is more susceptible to thermal noise than a digital circuit.

7.   Pulse Converter

One of the problems introduced by having DC motors is having a sufficient drive signal to turn the wheels when the input is chaotic. If the spike train is transformed into a constant DC voltage by a tachometer circuit, the random walk behavior is lost because the DC motor does not develop sufficient power to turn the wheels. This was overcome by converting the spikes into rectangle pulses with a mono-stable multi-vibrator circuit. This allows full-ON and full-OFF operation of the motor. The random walk behavior is translated into a stutter which is very effective at turning the vehicle.

8.   Motor Control Circuit

The pulses generated by the pulse converter are applied to the gate of a FET. This FET acts as a switch which powers the motor via a separate 3V battery power supply. The FET also acts as isolation between the noisy DC motor and the motor-controller electronics. The DC motors are very cheap and produce a great deal of sparking. The large capacitor acts as a filter to reduce some of that noise. With a better motor, most of the supporting filter circuitry could be removed.

9.   Results

The three Macro-Scale Robots successfully demonstrated random walk behavior in a variety of temperature and ambient light environments. They also demonstrated a stunningly efficient ability to detect a broadband light source, slew in the direction of that source and then move rapidly towards it while adjusting course to get both sensors to look straight at it. This hunting ability is ideal for swarming. The gradual transition between chaotic and periodic operation was also observed.

Flocking behavior was demonstrated by placing a light source on the back of one robot and letting another robot follow it. When the lead robot's random walk shined its

51

light source away from the trailing robot, the trailing robot transitioned back into random walk. In the presence of a swarm, this behavior will keep the group coherent.

One design consideration was that the trailing robot would tailgate the lead robot because it was moving faster due to a higher pulse frequency. This undesirable behavior was eliminated by mounting the sensors in such a way that there was a detection dead zone directly in front of the robot. Figure 46 illustrates this concept.
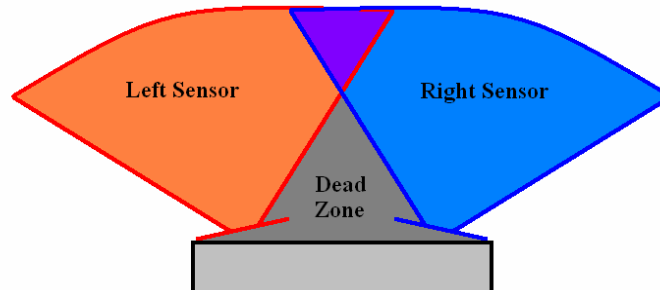
Figure 46.   Sensor placement requires a shallow dead zone in front to counter the tailgating effect of one robot directly behind another.

Proof of concept for pulse mode optical detection and processing was achieved. The success of the macro-robot design paves the way for MEMS based micro-robot design and provides lessons learned for future work.

C.   MICRO-SCALE ROBOT SWARM

Micro-robotics requires simplicity of design and adaptability to the environment. This can be accomplished through the use of a distributed processing network. Individual robots have access to local information but interact with each other to produce a global behavior. The archetype for this model can be found in the theoretical work of emergent behavior theory [10]. The key enabler of a micro-robotic design is the integration of CMOS and MEMS in a monolithic structure. The electrical and mechanical properties of a $300\,\mu$m micro-robot can be successfully simulated and evaluated for application to swarming logic with finite element analysis.

1. Simple Logic

The motivation for creating a micro-robotic swarm is to demonstrate the capability of a simple logic circuit in developing a distributed processing system. The circuit consists of a thyristor in series with a parallel capacitor and resistor circuit. Figure 47 shows a schematic of the circuit. Note that the output is across the thyristor itself.
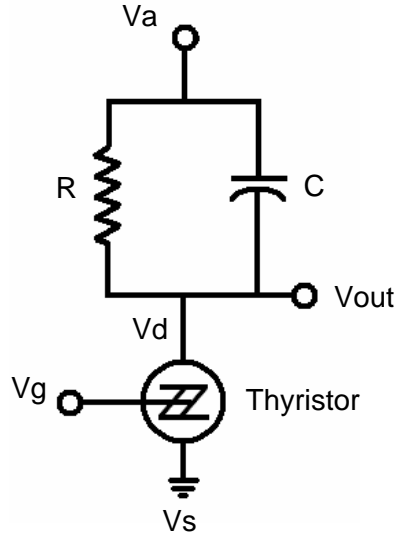
Figure 47.   Thyristor circuit.

Figure 48 shows typical outputs of the logic circuit.
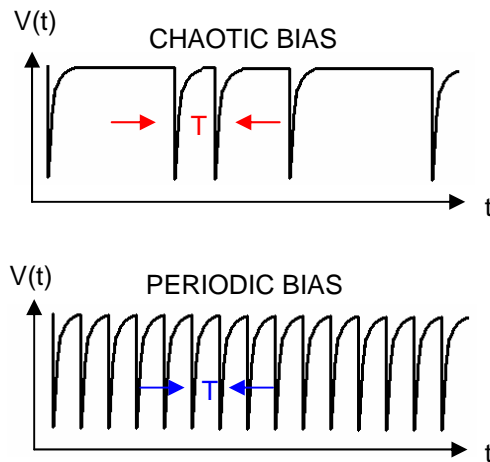
Figure 48.   Typical output.

The spectrum of operation between chaotic and periodic pulse rates can be used to produce the required logic for the robot to swarm. It accomplishes this by biasing the thyristor circuit based on sensory input. The robot has a sensor on each side that applies a voltage to the gate of a thyristor circuit used to drive a leg bank on the opposite side. In the absence of light, the leg bank will operate chaotically. In the presence of light, the leg bank will operate periodically and turn towards the light source. Both leg banks operate independently. Figure 49 shows the layout of the micro-robot design (the robot is upside down in the picture).

It is important to note that the circuit configuration was chosen to keep the legs grounded. This allows the legs to make contact with surfaces that are not insulators. This is of importance if the platform is used as a weapon against electronics.
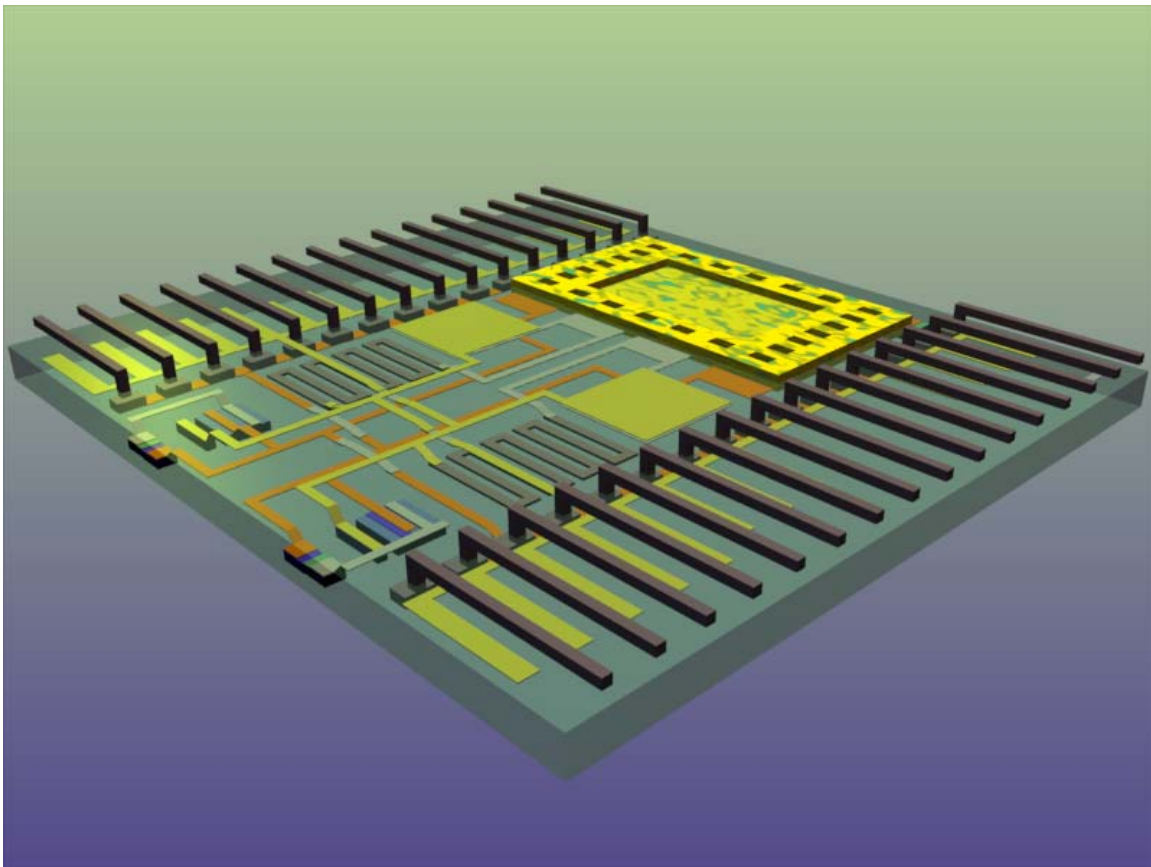
Figure 49.   Micro-robot design.

The design has an LED in the back of the robot. When other robots see this light source, they turn towards it. This characteristic allows flocking. If the robots can also sense a human light source, then the ones closest will turn towards the human. The ones behind them will turn towards the ones in front. The ones behind them will turn and so on. The end result is a swarm.

The power supply is a critical design feature. The current state of the art power supply is Radio Isotope Micro Power Sources (RIMS) technology, which is ideally suited for use in high-energy, low power applications. The power supply will be used to slowly charge a capacitor, and the capacitor will discharge with current suitable for switching of the thyristor. This design concept has already been successfully implemented in the macro-scale model as discussed in section III.B.

2. Fabrication Process

The micro-robot design incorporates both CMOS and MEMS onto a single structure. The electronics components will be fabricated on the assumptions of the SOI-SCMOS process that is available from MOSIS [17]. The advantage of this process is that is multi-user and therefore has a low cost of fabrication. Figure 50 shows the SCN3M CMOS process layers that are available for the design. All of the layers are used.

Figure 50.   SCN3M CMOS process.

The structural components will be fabricated by adding additional layers of oxide and poly-silicon via a custom post-CMOS MEMS process similar to IMEMS [18]. Figure 51 shows the custom MEMS process.
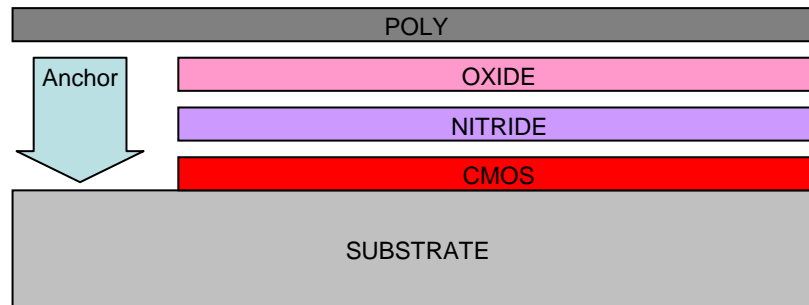
Figure 51.   MEMS process.

The nitride layer acts as a barrier to prevent the CMOS oxide from being etched when the MEMS oxide is released. An important consideration is the stresses inherent in the poly-silicon leg structure. Because the MEMS process is a follow on to the CMOS process, th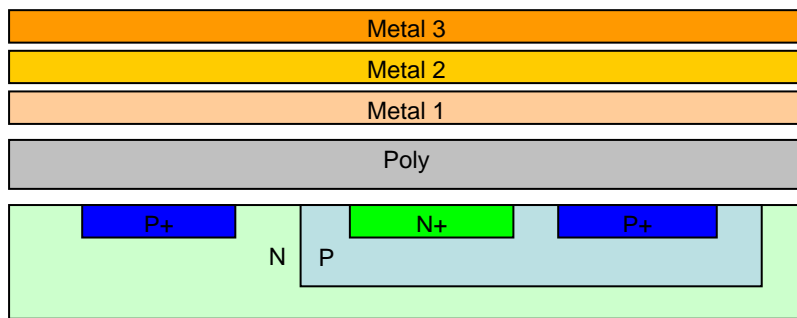e temperature used for annealing must be low enough to prevent damage to the CMOS metals and oxide. This requires careful management of the stress gradients so that the legs bend away from the substrate with the minimal possible deflection. Another mitigating factor is that the leg is 3 µm above the CMOS structure, so some bending is acceptable.

The final step will be to deep RIE etch around each robot and then release the top of the SOI wafer. The proof of concept that the micro-robot can operate its legs according to a swarming logic is immediate the goal. Therefore, the integration of a RIMS power supply and a GaAs LED will not be accomplished in the first fabrication run.

The micro-robot is required to demonstrate an ability to move according to sensory inputs. This will be accomplished by using PN diodes as light sensors to bias the thyristors for chaotic or period pulse mode operation. These thyristor pulses will be used to pull-in and release the leg structures in order to allow the robot to hop. The legs will be pulled forward as well as up so that the momentum of the released leg moves the robot up and forward.

3.   Finite Element Simulation

Both the electrical and mechanical properties of the micro-robot design were modeled in COMSOL, a multi-physics finite element program. The fabrication layout file

was generated in LEDIT using the SCN3M design rules for CMOS processing. Additional layers were added to the SCN3M layout in order to add the custom CMOS process.

The two important design considerations in the micro-robot are the leg banks and the thyristor circuits. The leg banks are an electro-mechanical system and the thyristor circuit is a solid state electronics system. Each of these systems was evaluated analytically and then modeled using finite element analysis.

4.   Leg Structure

The leg banks were designed according to the requirement that the applied voltage on the pull-in capacitor created sufficient deflection of the leg to allow the robot to move forward. The analytical model uses a balance of forces equation for the spring force of the beam and the Maxwell force of the capacitor. The standard force balance equation for a cantilever beam as follows [19]:

$$-\frac{Ebh^3x}{4L^3}+\frac{\varepsilon AV^2}{2g^2}=0 \tag{3.1}$$

The electrical circuit is capable of applying a 16 V bias to the leg actuator capacitor which can then be rapidly decreased to 0 when the thyristor turns on. When the thyristor turns back off again, the voltage slowly builds back up to 16 V. The result is that the 16 V is applied over a long period of time and the leg is able to come to a stable, fully cocked position. When the thyristor turns on, the leg is almost instantly released and the spring force of the beam drives the end of the leg down without the opposing Maxwell force to slow its decent. The momentum of the collision with the ground drives the robot up and forward in a hop.

For a 100nm deflection of a $100\,\mu$m x $1\,\mu$m x $1\,\mu$m beam and a 50 μm long capacitor plate, the applied bias voltage can be calculated analytically to be 22.1 V. This is close to the desired voltage of 16 V. Figure 52 shows the result of finite element analysis for three different size capacitors for an applied voltage of 16 V.
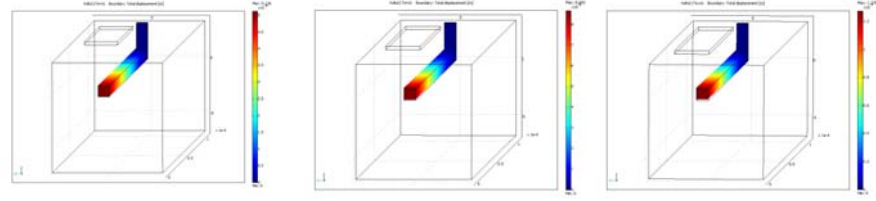
LENGTH OF CONTROL CAPACITOR	$40 \times 10^{-6} m$	$50 \times 10^{-6} m$	$60 \times 10^{-6} m$
DISTANCE OF TOTAL DISPLACEMENT	$5.1 \times 10^{-8} m$	$8.7 \times 10^{-8} m$	$1.3 \times 10^{-7} m$
CAPACITANCE OF LEG ASSEMBLY	$6.4 \times 10^{-16} F$	$7.8 \times 10^{-16} F$	$9.3 \times 10^{-16} F$

Figure 52.   Beam deflection calculation for different size capacitor plates.

The actual jump height of the micro-robot can be calculated analytically using conservation of energy. The following is the energy balance equation [19]:

$$\delta z = \frac{1}{M|\vec{g}|}\left[\frac{1}{2}\left(\frac{E_{Si}bh^3}{4L^3}\right)x^2\right] = \frac{1}{2M|\vec{g}|}\left(\frac{\varepsilon AV_s^2}{2g^2}\right)x \qquad (3.2)$$

For 16 V applied and 50 legs with an average capacitor plate length of 50um and a 100nm deflection, the jump height can be computed to be $0.67\,\mu m$.

Three different sized capacitor plates are used. In the front the plates are 60 μm, in the middle they are 50 μm and in the back they are 40 μm. The reason is that the extra energy in the forward legs causes the front of the robot to tilt up. This causes the rear end to hit the ground first and give greater obstacle clearance height.

The COMSOL model of the electro-mechanical leg system was created using Structural, Electrostatic and ALE models. The structural model computed all of the bending stress and added the Maxwell force generated in the electrostatic model to get a total beam deflection. The ALE deformable mesh model allowed the electrostatic and mechanical systems to be coupled without having to use an iterative solver routine. This is a very powerful technique for multi-physics coupling.

5.   Thyristor Circuit

The thyristor circuit was first modeled analytically by determining the required capacitor and resistor values for a given switching voltage to produce the correct bias for

chaotic operation. The resistance was chosen to bias the thyristor circuit at the switch point of the IV curve. The following relationship was used to determine the required value of the resistance, $16k\Omega$:

$$\frac{V_{Holding}}{I_{Holding}} < R < \frac{V_{Switch}}{I_{Switch}} \tag{3.3}$$

The capacitance was chosen to hold more charge than the reverse biased junction of the thyristor. The following equation was used to determine the value of the capacitance, $8.5 \times 10^{-13} F$:

$$C_{Thyristor} < \frac{\varepsilon_{Oxide} A_{Capacitor}}{g_{Capacitor}} \tag{3.4}$$

The capacitance of the thyristor was determined from finite element modeling with COMSOL. It is important to note that the capacitance of the leg assembly is much less than that of the circuit capacitor, so it will have a minimal effect on the biasing of the thyristor circuit.

The doping and dimensions of the thyristor were taken from thesis work completed by David Moore [16]. These characteristics were used to model the electrical behavior of the thyristor under an applied voltage and to determine the switching voltage of the device. The COMSOL model of the solid state thyristor circuit was created using Electrostatic and Diffusion models plus an ODE to simulate the external circuit. The Electrostatic model computed the potential across the device and the diffusion model calculated the electron and hole concentrations in the device. Figure 53 is a cross-section plot of the hole concentration across the thyristor. The drain is on the left, the source is in the middle, and the gate is on the right. The depletion region can be clearly seen where the blue line is. The contour lines represent potential.
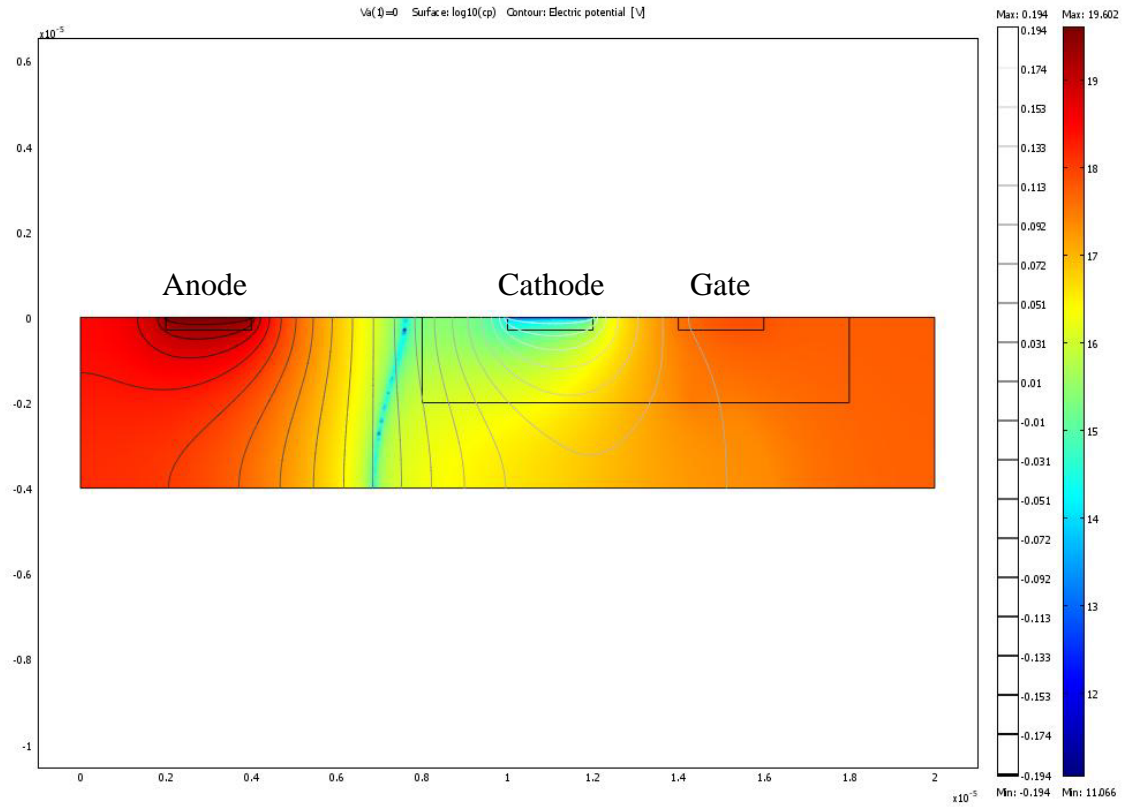
Figure 53.   Cross section of hole concentration in a thyristor device with no bias applied. The contour lines represent built-in electrostatic potential.

The switching voltage was predicted by COMSOL to be 16.1V. Figure 54 shows a plot of the voltage across the device. The middle PN junction is reversed biased as expected.
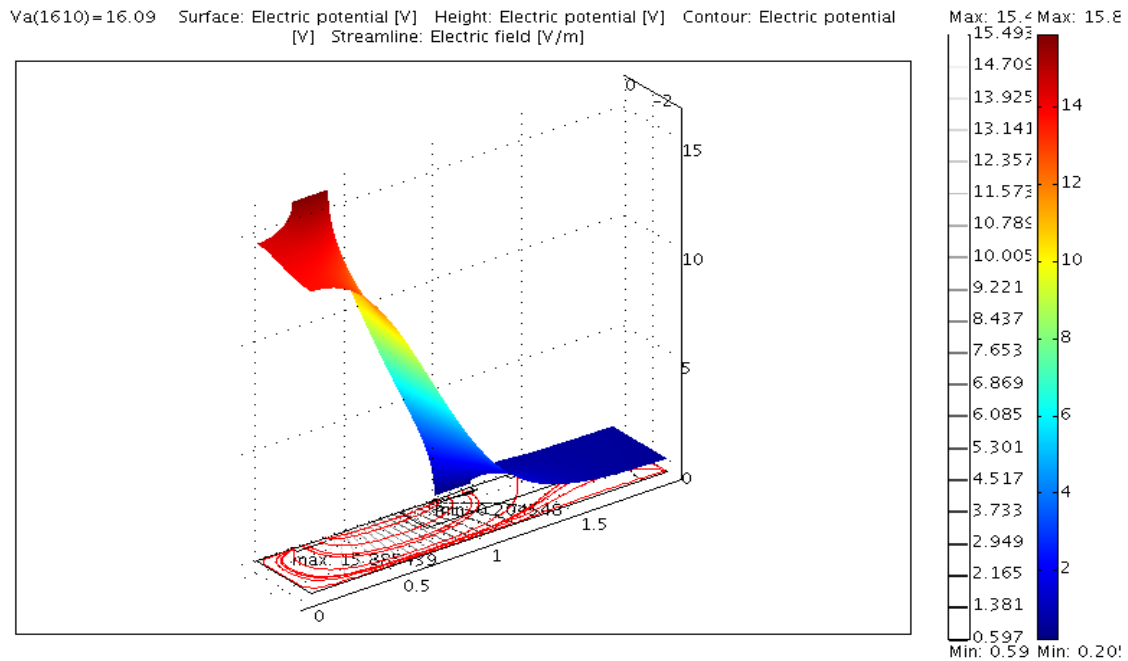
Figure 54.   Height and surface coloring reflect electrostatic potential across the thyristor for 16.01 V applied to the anode. The red lines are electric field.

Figure 55 shows the current as a function of the applied voltage. The solution stops converging at the switching voltage.

Figure 55.   I-V characteristics of the thyristor. Units are $A/\mu m$.

61

6. Results

The analytic and finite element analysis was used to generate a layout for the micro-robot in LEDIT. The length of the thyristor required was made to be $32\mu m$ which results in a switching current of $51.2\mu A$. Th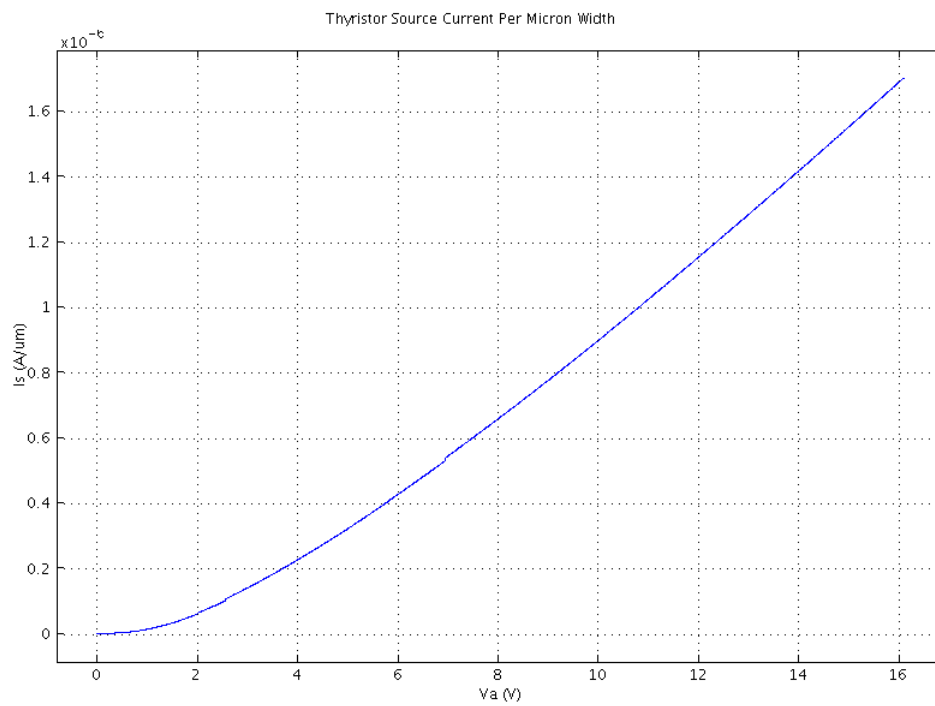e resistance value required for the circuit bias was then determined to be $16k\Omega$. This translates to 484 squares of CMOS poly. Finally, the CMOS metal capacitors needed to be $50\mu m \times 50\mu m$ in order to have a capacitance of $8.5 \times 10^{-13} F$. The final dimensions of the micro-robot are $290\mu m \times 310\mu m$. Figure 56 shows the LEDIT layout that will be used for fabrication.

LEGS
THYRISTOR
RESISTOR
CAPACITOR
PN DIODE
POWER
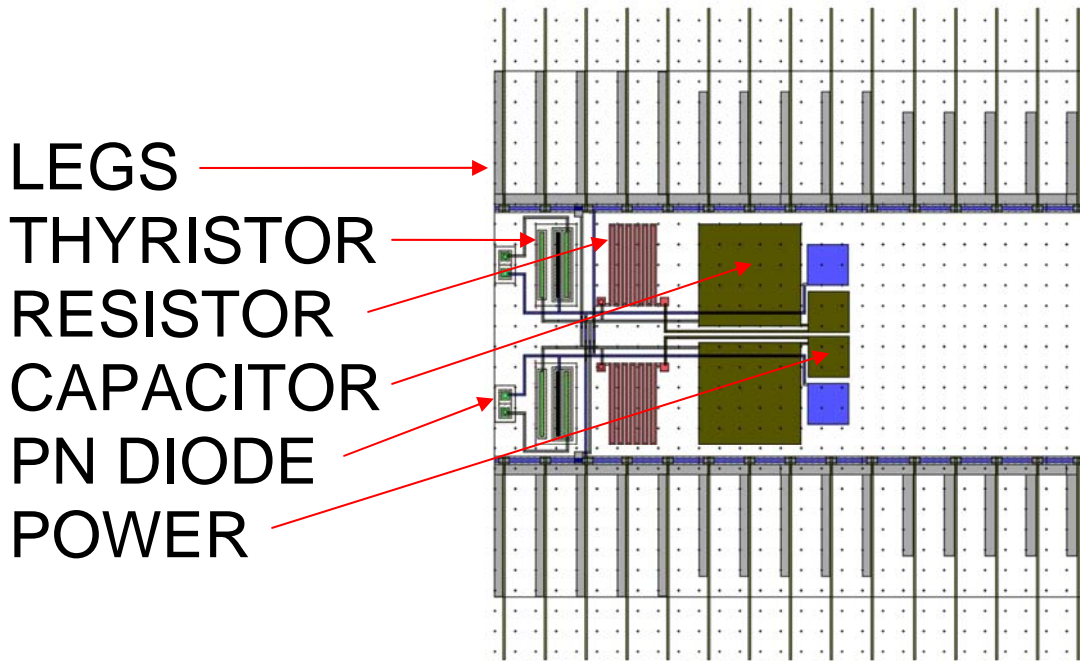
Figure 56.   LEDIT layout using SCN3M rules and custom MEMS layers.

The fabrication of a micro-robot platform that is capable of swarming is possible. The first step is to have a working electro-mechanical system. A CMOS/MEMS process can be used to create that system. Follow on work will integrate a RIMS power supply and a GaAs LED light source so that the platform is totally autonomous.

There are a number of hurdles yet to overcome. The first is to ensure adequate electrical isolation between thyristor circuits. The second is to overcome inherent stresses of MEMS fabrication. The third and most difficult is to ensure that the thyristor is

correctly biased for chaotic operation at room temperature. With these challenges met, the future of emergent behavior micro-robotics is bright. A swarm of micro-robots can penetrate and destroy electronics, collect hazardous materials, form self-assembling structures, transmit targeting data and perform many other useful applications.

THIS PAGE INTENTIONALLY LEFT BLANK

IV.   CONCLUSIONS AND RECOMMENDATIONS

It was determined that the behavior of the thyristor pulse generating circuit is described by the Poisson Point Process statistical model:

$$P(t) = \begin{cases} \dfrac{e^{\frac{t_0}{\langle t \rangle - t_0}}}{\langle t \rangle - t_0} e^{\frac{-t}{\langle t \rangle - t_0}}, & t > t_0 \\ \\ 0, & t \le t_0 \end{cases} \qquad (2.27)$$

The mean time interval is related to temperature and voltage bias by the following:

$$\langle t \rangle = \tilde{t}_0^{\; -\frac{q}{\eta kT}\left[V_{DC} - V_P e^{-\frac{\langle t \rangle}{RC}} \right]} \qquad (2.7)$$

The refractory period t_0 is related to the RC time constant of the circuit:

$$t_0 = RC \qquad (2.25)$$

Thus, the pulse rate and variance of the distribution can be controlled by the proper application of voltage bias. It was also observed that the injection of current into the gate produces the same effect as increasing the bias voltage. PN Hook Theory offers a qualitative description of the behavior of the pulse generating circuit that suggests that current multiplication is highly sensitive to temperature and voltage bias.

A.   DISTRIBUTED PROCESSING

The thyristor circuit and a photo diode were implemented as an effective pulse mode optical detector capable of operation in both periodic and chaotic regimes. This circuit consists of four components and can be scaled in size to very small dimensions because of this simplicity.

The pulse mode optical detector behaves like a biological neuron and can be used for distributed processing logic in a neural network. This concept was successfully applied to a macro-scale robotic platform capable of emergent behavior swarming and was a key enabler of the micro-robotic swarm design.

A micro-robotic platform capable of swarming is easily attainable using current MEMS/CMOS/RIMS fabrication methods, and is far from cost-prohibitive. The proposed

swarming platform is highly adaptive to a changing environment and can be easily adapted for specialized missions because of the simplicity of the design.

B.   FUTURE WORK

The power of this distributed processing system is in its scalability. Future work should seek to apply the aperiodic pulse-mode logic to other micro-scale systems that are required to learn and adapt to the environment quickly.

The proposed micro-robotic swarm can be used as a weapon against electronics, collect hazardous materials, form self-assembling structures, and transmit targeting data. By changing the physical characteristics of the platform, it is not hard to imagine that this swarm could operate in the cold vacuum of space or in the harsh atmosphere of Mars.

Future work should be directed at making this swarm capable of other distributed processing tasks. The power of emergent behavior systems is that they are highly adaptable and can exhibit a variety of complex behaviors required for attaining and end-state. Some possible applications of the pulse generating circuit include a self-healing sensor network, neural enhancement in humans such as artificial vision for the blind, neural networks based on analog pulse-mode logic, and off-world terra-forming and space exploration.

The simplicity of the device and the complexity of its behavior suggest its applicability to the creation of neural network artificial life. This is an endeavor that should be seriously considered as a means to enhance human understanding of complex systems and enable humans to master the challenges of survival in the new century.

APPENDIX   MACRO-SCALE ROBOT SCHEMATIC
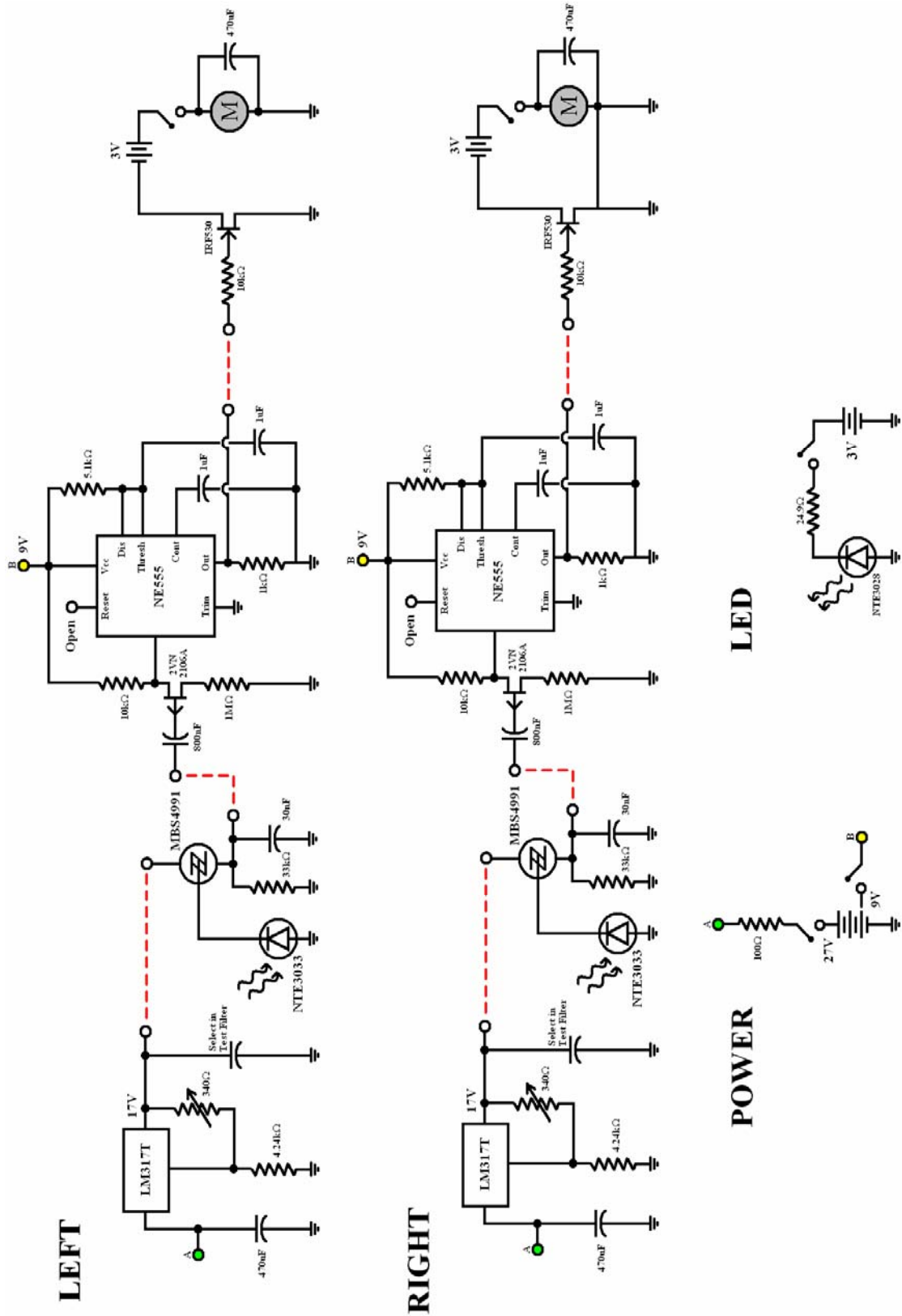
THIS PAGE INTENTIONALLY LEFT BLANK

LIST OF REFERENCES

1. Gamani Karunasiri, "Spontaneous Pulse Generation Using Silicon Controlled Rectifier," *Applied Physics Letters*, Vol. 89, pp.1-3, 2006

2. W. Shockley, Electrons and Holes in Semiconductors with Applications to Transistor Electronics, D. Van Nostrand Company, Inc., NY, 1950, pp.111-113

3. Motorolla MBS4991/4992/4993 Technical Data Sheet, Motorolla Semiconductor, Inc., www.motorolla.com, last accessed 1 July 2006.

4. N. Y. S. Kiang, T. Watanabe, E. C. Thomas, and L. F. Clark, *Discharge Patterns of Single Fibers in the Cat's Auditory Nerve*, Cambridge, Mass.: M.I.T. Press, 1965.

5. Richard A. Greiner, *Semiconductor Devices and Applications*, McGraw-Hill, NY, 1961, p.122

6. David Heeger, FTP document "Poisson Model of Spike Generation," 05 Sep 2000, pp.4-5, www.cns.nyu.edu/~david/ftp/handouts/poisson.pdf, last accessed 30 July 2006

7. MATLAB Online Help File: "Power Spectral Density," MATLAB 7.1 Software, The MathWorks, Inc, 1994-2005

8. R.C. Hilborne, *Chaos and Nonlinear Dynamics*, Oxford University Press, Oxford, U.K., 1994

9. MATLAB Online Help File: "xcorr (Signal Processing Toolbox)," MATLAB 7.1 Software, The MathWorks, Inc, 1994-2005

10. Steve Johnson, *Emergence: The Connected Lives of Ants, Brains, Cities and Software*, Scribner, NY, 2001

11. Website: "Home Page of John Koza," http://www.genetic-programming.com/johnkoza.html, last accessed 1 Aug 2006

12. Andrew Ilachinski, *Irreducible Semi-Autonomous Adaptive Combat (ISAAC): An artificial Life Approach to Land Warfare (U),* Center for Naval Analyses, Alexandria, VA, 1997

13. Website: "Neural Network," http://en.wikipedia.org/wiki/Neural_network, last accessed 1 Aug 2006

14. Greg Kirkpatrick, Webpage: "Marathon's Story," http://marathon.bungie.org/story/rampancy.html, last accessed 1 Aug 2006

15. David A. Moore, "Optical Detection Using Four-Layer Semiconductor Structures," Naval Postgraduate School, Master's Thesis, June 2005

16. Joseph W. Goodman, *Introduction to Fourier Optics*, 3rd Ed., Roberts and Company, Englewood, Colorado, 2005

17. FTP Document: "MOSIS SCMOS Design Rules," MOSIS, http://www.mosis.org/Technical/Designrules/scmos/scmos-main.html, last accessed 1 Aug 2006

18. J.H. Smith, et. all, "Embedded Micromechanical Devices for the Monolithic Integration of MEMS with CMOS," Sandia National Laboratories, Proc. 1995 IEDM, pp.609-612

19. Stephen D. Senturia, *Microsystem Design*, Kluwer Academic Publishers, Boston, MA, 2001

INITIAL DISTRIBUTION LIST

1. Defense Technical Information Center
   Ft. Belvoir, Virginia

2. Dudley Knox Library
   Naval Postgraduate School
   Monterey, California

3. Professor Gamani Karunasiri, Code PH/Kg
   Naval Postgraduate School
   Monterey, California

4. Dr. Richard Waters, Code 2876 (MEMS)
   SSC-SD
   San Diego, California

3. Mr. William G. Glenney IV, Deputy Director CNO Strategic Studies Group
   Naval War College
   Newport, Rhode Island